FINITE ELEMENT ANALYSIS OF RAILWAY TRACK UNDER VEHICLE DYNAMIC IMPACT AND LONGITUDINAL LOADS

BY

ZIJIAN ZHANG

THESIS

Submitted in partial fulfillment of the requirements
for the degree of Master of Science in Civil Engineering
in the Graduate College of the
University of Illinois at Urbana-Champaign, 2015

Urbana, Illinois

Advisor:

Professor Bassem O. Andrawes

ABSTRACT

Impact loads caused by flat spots on railcar wheels impose a major maintenance burden on railroads and can cause severe damage to both railcar and rail track components. In addition, the increasing tractive power of locomotives leads to significant increase in the longitudinal load demand in railway tracks. The capacity of longitudinal restraint of existing rail fastening system and its dependency on track parameters affects the future design of rail fastening system. This thesis focuses on investigating numerically these two problems using finite element (FE) method. An FE model with multiple crossties and their accompanying fastening systems is developed and utilized in this study after being validated using field data. The results of the impact load study indicate that impact loading consists of direct wheel impact loads and track system vibration induced impact loads. Both of these impact mechanisms are sensitive to the parameters considered in this study, including the stiffness of rail pad and the speed of train. It is observed that rail pad with a moderate stiffness provides the most effective impact attenuation. Furthermore, impact load is found to increase with increasing train speed.

On the other hand, the study conducted on longitudinal track loads focused on investigating the effects of wheel acceleration, elastic modulus of clips, rail-to-railpad coefficient of friction (COF), and crosstie spacing on the distribution of longitudinal force in the rail fastening system. The FE model results suggest that a coefficient of friction (COF) of 0.65 is most efficient in maximizing the longitudinal restraint per railseat. Additionally, a crosstie spacing of 24 inches can lead to a desired distribution of longitudinal force.

to father and mother,

for always supporting me

致我的父母，

感谢你们无私的支持

ACKNOWLEDGEMENTS

Last but not least, I would like to thank my family. My mom and dad. You have been giving my unconditional support and love. I would have never come so far with my academic career without your supports.

TABLE OF CONTENTS

CHAPTER 1

INTRODUCTION

1.1.   Motivation

The advancement of technology in the manufacture of trains, mainly both higher

operating speed and heavier axle loads is essential to satisfy the growing demand for passenger

transit and freight. This rapid development in modern rail vehicle greatly improves the power

and speed of trains, yet it imposes increasing performance demand on the railway track system.

The heavy freight and high speed passenger trains can cause much higher traffic loads that

exceed the design strength and capacity of current railroads. For example, the deployment of

heavier and faster trains will result in the increase in impact loads and longitudinal forces, which

can potentially compromise the structural reliability of track components. In other words, the

dynamic vehicle loads can be much amplified. Vertical dynamic loads in the railway track can be

attributed to both the vibration interaction between the wheel and rail (Kaewunruen &

Remennikov, 2010) and the irregularities of the wheel and rail (Kumar & Sambasivarao, 2014).

A more severe vertical dynamic load is typically associated with the presence of wheel and rail

irregularities such as wheel flats and insulating rail joints (Nielsen, 2008); the latter is typically

known as the impact load. Previous records in North America have shown that the impact loads

can exceed the static load by 2.5 to 3.5 times, and therefore pose a critical concern regarding the

reliability of track components (Zarembski & Bell, 2002). Impact loads are hazardous to the

track structure as they may cause cracking in the crossties and accelerate the degradation of track

geometry, and thus lead to large maintenance expense (Zarembski & Bell, 2002).

In addition to the impact load, the increasing longitudinal load due to more powerful trains is another concern for the track structure. With the increasing use of continuously welded rail (CWR), the longitudinal load is even of more importance. The CWR, unlike conventional joint rail, allows for the rail segments to form an uninterrupted section. The absence of joints offers several advantages including increased passenger comfort, reduction in audible noise caused by train passage, reduced rate of deterioration of track, and reduced dynamic effects associated with the existence of joints (Carvalho et al., 2013). Nevertheless, the effects of longitudinal load can be much exacerbated as the allowance for the longitudinal movement of rail by the rail joints is deprived in the CWR.

The longitudinal load in CWR is commonly induced due to the uniform temperature change of the rail, tractive effort of the train, and sudden change of stiffness of the supporting structure (Ruge & Birk, 2007). The latter two, cause localized longitudinal stress along a finite length of the rail whereas the uniform temperature change induces longitudinal stress along a much longer section. While all three causes can lead to buckling of rail, longitudinal load due to the vehicle tractive effort possesses a higher degree of uncertainty as it is unique to every train consist. Furthermore, it is likely to undergo significant increase as the rail vehicle technology advances. The resistance to longitudinal load and movement of rail is provided by rail fastening system which anchors the rail to the crossties (AREMA, 2014). Therefore, the capacity of rail fastening system for longitudinal resistance is an important reference for the longitudinal stability of track structure.

In addition to the continuous increase in load demands, the last few decades have witnessed a shift away from the use of timber crossties to the use of concrete crossties in new construction of railroads. This shift is primarily due to the scarcity of timber and its increasing

price (National Academy of Sciences (U.S.), 1976). However, the current design specifications practiced in the United States for railway tracks with concrete crossties is derived from empirical design process primarily developed for timber tie track system (Van Dyk, 2013). As a result, the service life of track components is likely reduced, leading to more frequent maintenance and thus higher costs. Therefore, the response of concrete-crosstie track system to complex loading environments needs to be investigated.

1.2. *Thesis Scope*

This study investigates numerically the behavior of impact load caused by wheel flat in concrete crosstie tracks. The study will shed the light on the relationship between the impact force and track design parameters. In addition, the study examines the distribution and magnitude of longitudinal force in the concrete crosstie fastening system and their relationships with track design parameters. The study is carried out numerically using finite element (FE) analysis. Two detailed 3D FE models were developed, validated using field data, and utilized in the study.

1.3. *Thesis Outline*

Chapter 2 provides background on railway track system, in particular concrete crosstie track which is the focus of this study. It also introduces two major hazards in a concrete crosstie track, that is, large longitudinal and impact loads. In addition, it also contains information from literatures on the cause of longitudinal and impact loads and their associated damaging mechanisms.

Chapter 3 elaborates on the development of the finite element (FE) model for analyzing track response to dynamical impact load. It discusses the modeled track components and their

material properties, contact interaction properties defined for track components, and the loading procedure used for the FE analysis.

Chapter 4 introduces the validation of the FE model using field data. It introduces the setup and instrumentation of the field test and the parameters used to validate the FE model.

Chapter 5 introduces the second FE model that was developed to analyze the track response due to wheel induced longitudinal load.

Chapter 6 presents the results of the validation of the second FE model using field collected data.

Chapter 7 presents parametric study results from both FE models and discusses the observations associated with each parameter.

Chapter 8 includes the summary and main conclusions of the study as well as brief recommendations for future work.

CHAPTER 2

BACKGROUND AND LITERATURE REVIEW

2.1. *Concrete Crosstie Fastening Systems*

A railway track is a sophisticated system comprising multiple components, and the

strength of each track component is liable for the structural integrity of the whole track system.

The connection between the rail and concrete crossties is provided by the fastening system which

consists of multiple track components (Esveld, 2001). The functions of a concrete crosstie

fastening system include providing and maintaining various degrees of gauge restraint, transfer

of vertical, lateral, and longitudinal loads from rail to crosstie, load or impact attenuation, and

electrical isolation (AREMA, 2014). There are two major types of fastening systems for concrete

crosstie tracks: screw systems and clip systems (Kerr, 2003). Compared to clip systems, screw

systems possess certain disadvantages as they require more maintenance and the clamping force

produced can vary among railseats (Kerr, 2003). In North America, four types of clip fastening

systems are commonly used with concrete crossties. As illustrated in Figure 2.1, these include

the e-clip, the Safelok I and III, and the Fastclip (Kerr, 2003).
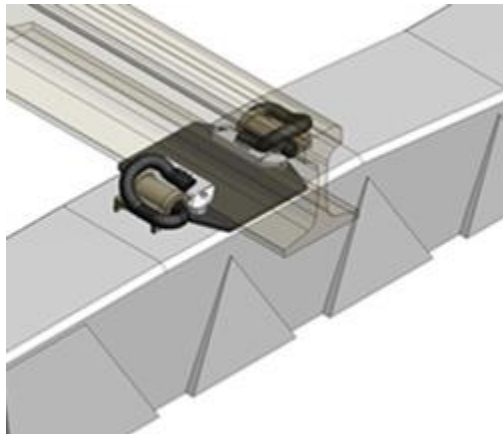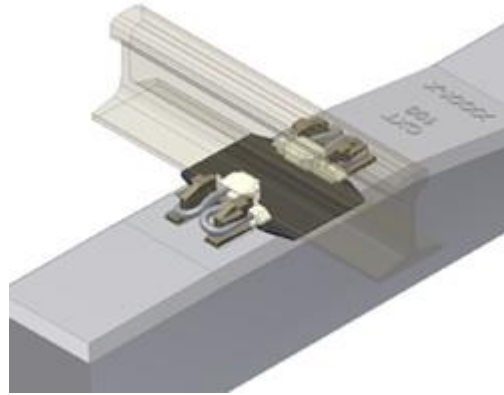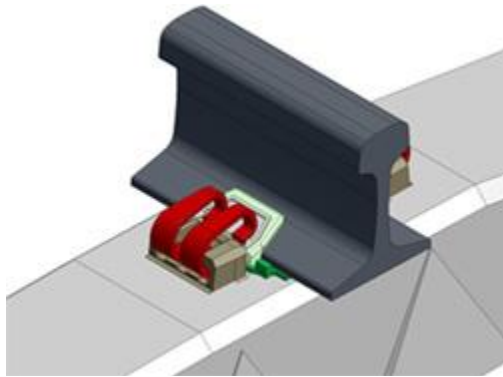
E-Clip	Fastclip
Safelok I	Safelok III
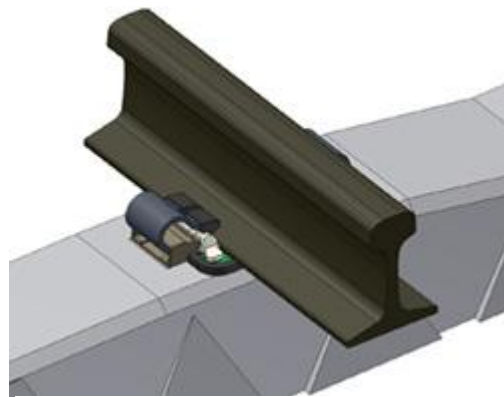
Figure 2.1. Concrete Crosstie Fastening Systems (adapted from CXT Concrete Crossties)

The fastening system considered in this study is the Safelok I system. It includes a pair of spring clips, insulators and shoulders and a rail pad assembly. The spring clips exert clamping forces on the rail which control longitudinal rail movement due to thermal and tractive forces and minimize rail gap in the event of a rail break (AREMA, 2014). The insulators serve to prevent interference with signal system and deterioration of the fastening system through electrical leakage (AREMA, 2014). The shoulders is a cast-in component that provides anchorage points within crossties for rail fastening systems and other miscellaneous components (AREMA, 2014). The rail pad assembly consists of a rail pad and an abrasion plate and is

installed between the rail and concrete crossties to reduce impact and vibration effects on the track structure and minimize railseat deterioration (AREMA, 2014).

Figure 2.2 illustrates the fastening components of the Safelok I fastening system. The shoulder is designed to hold the clip to the tie and is cast-in during the manufacturing process of crosstie (Romero et al., 2010). The pair of legs (stems) at the bottom of the shoulder bond with the concrete crosstie, producing resistance to pull-out and ensuring stability of the connected fastening components (do Carmo, 2014). The spring clip is driven into the shoulder and exerts a clamping force by its elastic deformation. The clamping force per railseat produced by spring clips can range from 4,400 lbs to 5,800 lbs for the common types of concrete crosstie fastening system in North America (Romero et al., 2010). The Safelok I fastening system can provide 4,800 lbs clamping force (Romero et al., 2010). The insulators on the field and gauge sides have different geometries. They are commonly made from nylon 6/6 which possesses high mechanical strength and good abrasion and high temperature resistance (do Carmo, 2014). The railpad is also made from polyurethane. As polyurethane is a soft material, it is expected to provide good attenuation for contact interaction between the rail and crosstie caused by dynamic impact. The abrasion plate, on the other hand, protects the railseat against mechanical wear and prevents sawing action from the longitudinal rail movements (Hay, 1982).
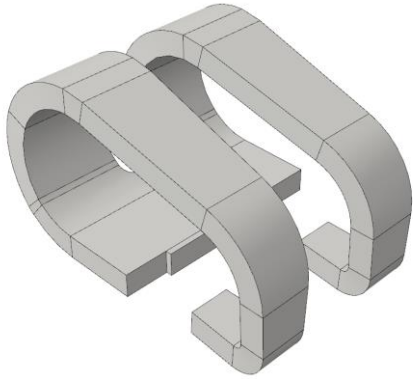
Spring Clip
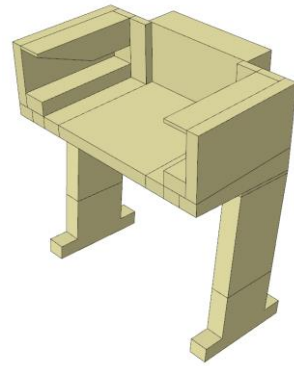
Cast-in Shoulder
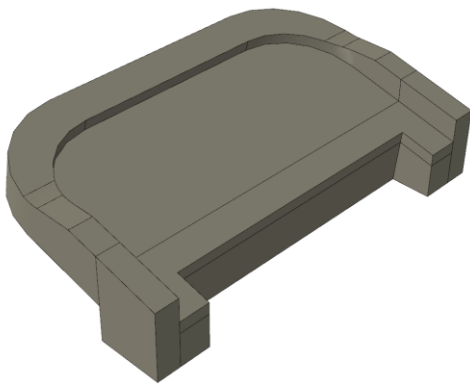
Field-side Insulator
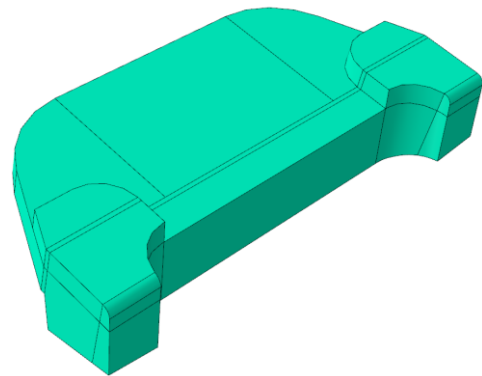
Gauge-side Insulator
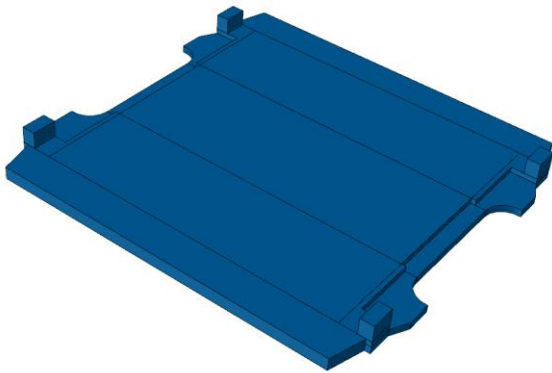
Rail Pad
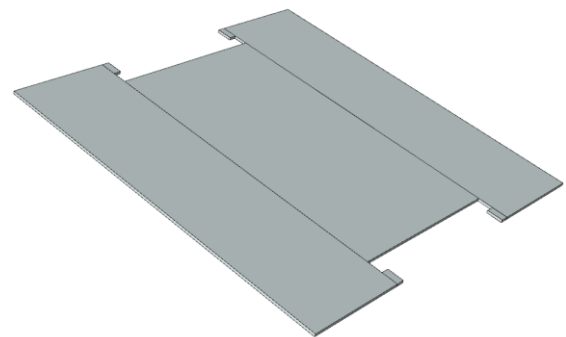
Abrasion Plate

Figure 2.2. Safelok I Fastening System Components

2.2. *Background on Impact Load*

One of the hazards of impact loads to track system is the damage to track components, predominantly being the cracking of crossties. Kaewunruen and Remennikov (2010) suggested that the train-track interaction and its resulting resonance in track components were the primary causes of large impact forces. Compared to the dynamic force due to general dynamic wheel-rail interactions, which has low magnitude but high cycle, the impact force has much higher magnitude but lower cycle and is more damaging to prestressed concrete crossties (Ye et al., 1994; Wang, 1996; Wakui & Okuda, 1999; Gustavson, 2002; Stevens & Dux, 2004). Even though the high magnitude impact load has been recognized as damaging to concrete crossties, the failure of a concrete crosstie is more likely to occur due to cumulative damage rather than due to a single occurrence of impact load (Kaewunruen, 2007; Kaewunruen & Remennikov, 2009). Therefore, it is crucial to assess the threshold of the value of impact load that can result in cumulative damage of concrete crosstie.

In addition to impact load in perfectly supported tracks, uneven support conditions for concrete crossties in the field is not a rare occurrence especially after the reworking of ballast. And the presence of voids under concrete crossties is likely to ease the excitation of vibration modes of concrete crossties. In such events, impact loads are believed to be excessively large.

One of the primary causes of dynamic impact loads in a railway track is the rail wheel flat spots. The formation of a wheel flat is generally attributed to the braking of a train. Braking slows the rotation of wheels and can cause the wheels to slide along the rails so that the train is decelerated by the friction between the wheels and rails. However, the sliding can wear off a portion of the wheel treads and result in a flat spot (Dukkipati & Dong, 1999). The size and shape of wheel flats, as well as wheel load and train speed are the factors that affect the impact load; and certain combinations of these factors can result in large impact loads that may cause

serious damage to track structures (Bian et al., 2013). In addition, as the magnitude of impact loads can be much higher than the cyclic loads from the passage of wheels, and the track components are prone to accelerated degradation under the effects of impact loads.

The determination of impact factor is typically highly simplified in practice. The American Railway Engineering and Maintenance-of-Way Association (AREMA) assumes an impact factor of 2.0 for the flexural design of concrete crossties. However, data acquired by wheel impact load detectors (WILD) on Amtrak at Edgewood, Maryland and elsewhere on freight railroads indicated that impact factors could easily exceed the 2.0 design value (Van Dyk et al., 2014). There were also instances of loads exceeding the 2.0 design value observed from passenger car wheels. These data suggest that the design impact factor be revisited to accommodate for wheel loads that exceed the current value of 2.0.

In addition, many studies in the past have presented different variations of formulas used to determine impact factors (Doyle, 1980; Van Dyk et al., 2014). While most formulas only relate the impact factor to train speed; other more comprehensive formulas also incorporated vehicle-related parameters, including wheel diameter, vehicle unsprung mass, etc.; and track-related parameters, including track modulus, cant radius, etc. (Van Dyk et al., 2014). However, most of the equations were empirically derived and independent of the types of rail and wheel defects, thus they shall not be used to predict impact loads caused by wheel flat.

In a study by Dukkupati and Dong (1999), an FE model was employed to investigate the characteristics of impact loads due to wheel flats and other defects. The railway track was modeled as a Timoshenko beam on discrete supports and the wheel flat was approximated by a haversine defect and grounded into the rail as an equivalent of a flat spot on the wheel. The use of a haversine defect on the rail might not represent the wheel defect at high speed as the

10

researchers realized that the wheel flew over the rail defect and resulted in small impact loads at high speeds. Also, as the FE model was in two-dimensions (2D) and linear constitutive relation was assumed for all components, the results may not capture the realistic nonlinear behaviors of the railway track system. Therefore, a three-dimensional (3D) FE model is needed to better investigate the characteristics of impact loads caused by wheel flats.

Bian et al. (2013) developed a 3D FE model which simulated the rolling of a railcar wheel on a three-crosstie railway track system. The FE model was used to simulate various magnitudes of impact loads at different speeds and at different static wheel loads. A symmetric boundary condition was enforced at the track centerline as only half of the track was modeled. Therefore, the FE model was only representative of symmetrical impact loading on both rails. However, as impact loading is typically asymmetrical, that is, only occurs on one rail, this FE model is incompetent in simulating realistic railway track behavior under impact loading. In addition, this FE model only included three railseats, which was fewer than the five railseats suggested by AREMA (2014) as the longitudinal distribution length for vertical wheel load.

An improved 3D model of a wheel-track system is presented in order to study the effects of impact loads due to wheel flats. It highlights a full railway track consisting of two rails, which allows the wheel flat to be presented on only one rail. In addition, a longer length of track was modeled, so that the distribution of railseat load can be correctly simulated. Field experimental data was used to validate the FE model. The FE modeling results are used for the investigation of the behaviors of impact loading with different system parameters which include the rail pad stiffness and train speed.

2.3.   *Track Buckling and Track Geometry Irregularity*

Track longitudinal loads cause significant concerns related to the lateral stability of the rail. In other words, excessive longitudinal loads could cause lateral buckling of the track. Track buckling is the formation of large lateral misalignments in CWR; it often results in catastrophic derailments. Buckling of the track is typically due the combined effect of three major factors: high compressive forces, weakened track conditions, and vehicle loads (Volpe, 2014).

High compressive forces are a result of a temperature raise above the rail neutral temperature of rail. The rail neutral temperature refers to the state wherein the rail is stress free in the longitudinal direction. It is typically the temperature at which the track is constructed. Therefore, if the ambient temperature rises above the neutral temperature, the rail is subjected to thermal expansion which then induces compressive stress. The problem associated with high thermal load is often addressed by installing the rail at a controlled temperature of 95-110 °F. As the temperature in the rail can reach 130-150 °F in some field conditions, the high neutral temperature prevents the rail from experiencing excessively high buckling forces (Volpe, 2014).

Weakened track conditions refer to reduced track lateral resistance as well as permanent track misalignment. Track lateral resistance is the reaction offered by the ballast against lateral movement. The track lateral resistance can be reduced by 40-70% due to surfacing and tamping of ballast, causing the rail to become buckling prone (Kish, 2011). In addition to the impaired track lateral resistance, track lateral misalignment is another cause for track buckling. As illustrated in Figure 2.3, for a perfectly aligned tangent track, a snap-through buckling mechanism prevails with increasing compressive stress in the rail. In other words, it is essentially the introduction of a small lateral deflection that causes the rail to snap-through from the perfectly aligned and unbuckled state to the buckling prone state. Once the misalignment is present in the track, its lateral resistance is significantly reduced (Figure 2.3).

12
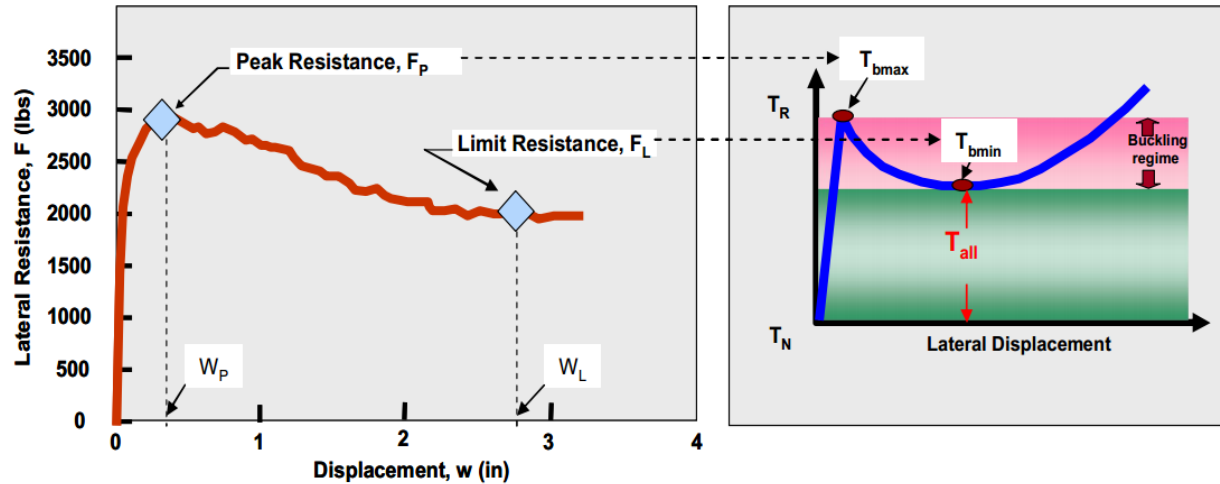
Figure 2.3. Peak and Limit Resistance Impacts on Buckling Temperature (adapted from Kish, 2011)

In tangent tracks, vehicle loads are often resulted from slack action, braking of trains, and rolling friction of trains. Slack action refers to the amount of free movement of one railcar before its motion is transmitted to a coupled car (UMKC School of Law, 1945). It is a source of track buckling as the tractive effort produced by a locomotive is at its greatest if a slack is present between the locomotive and trailing cars. The braking and rolling friction of trains cause track buckling in a similar way as they both exert localized longitudinal force in the rail. In curved tracks, buckling can also be triggered as large lateral force can be exerted on the rail (Williams et al., 2014).

2.4. *Longitudinal Loads in Railway Tracks*

Longitudinal forces in a railway track are produced by the tractive effort and dynamic braking of a train (Srinivas et al., 2011). As railway traffic demands exhibit a rapid increase over the past few decades in terms of their tonnages and speed of trains, more powerful locomotives have been built to meet the surging demands; the latest model of diesel-electric locomotive is

capable of producing twice as much tractive force as its predecessors (Foutch et al., 2006). As a result, the longitudinal forces imparted from the tractive effort are increased significantly. The longitudinal forces transfer from the rail to the crossties through the fastening system. In other words, the fastening system serves as the connection between the rail and the crossties, thus anchors the rail against its longitudinal movement due to forces in the longitudinal direction (Srinivas et al., 2011). Therefore, the increase in the wheel-induced longitudinal forces can impose a higher load demand in the fastening system.

The current design standard practiced in the United States by AREMA provides a single-tie and single-rail pullout test as the reference for the design and manufacture of rail fasteners (Figure 2.4). It states a threshold of 0.20 inch for the longitudinal displacement of the rail as an increasing longitudinal force, up to 2.4 kips, is applied to the rail and held for 15 minutes; and an additional longitudinal displacement of 0.01 inch cannot be exceeded after the force is held for three minutes. A similar test is described in the European standard (EN 2002), except for that the longitudinal load is increased until slippage occurs in the rail. As is conducted on a single railseat, the test specified in AREMA (2014) only accounts for a longitudinal force that is not greater than 2.4 kips per railseat. The value of 2.4 kips, according to AREMA (2014), is sufficient considering general service based on experience, but there are locations where excessive longitudinal forces are present. In addition, the test only applies to fasteners on crossties with 24-inch spacing. Therefore, the longitudinal load imparted in the railseat under various service conditions needs to be investigated.
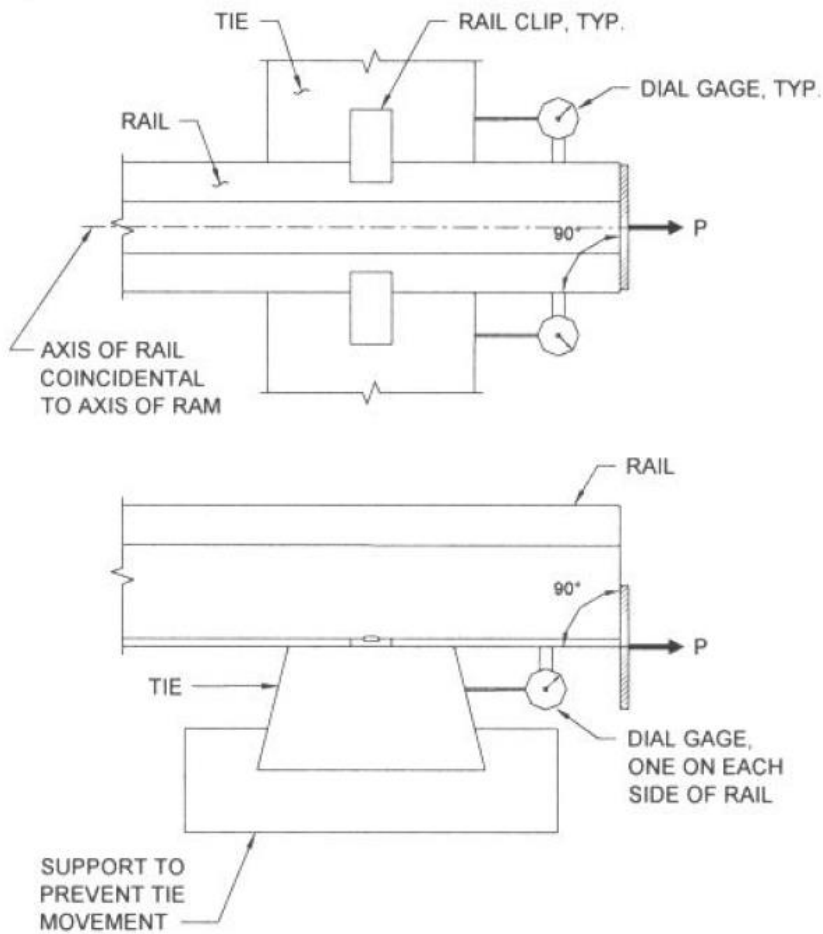
Figure 2.4. Fastener Longitudinal Restraint Test (AREMA, 2014)

In a field experimentation conducted by Srinivas et al. (2011), longitudinal force in a bridge track was investigated. The field experimentation concerns the scenarios that include the accelerating and braking of a train as well as the train running at uniform speeds. Based on the results of the experimentation, among the three testing scenarios, the highest longitudinal force is imparted in the rail under the passage of an accelerating train. Furthermore, a much more significant longitudinal force is induced by the locomotive wheel compared to the trailing car wheels (Srinivas et al., 2011). As illustrated in Figure 2.5, a locomotive wheel is driven by the

rotation of the axle while a trailing car wheel rolls due to the friction force between the wheel and the rail. For an accelerating train, part of the tractive forces is distributed as the friction forces between the trailing car wheels and the rail. However, as the number of the locomotive wheels is typically less than that of the trailing car wheels, larger longitudinal forces are produced by locomotive wheels. Therefore, an accelerating locomotive wheel is of most importance to be investigated concerning the longitudinal force imparted in the fastening system.
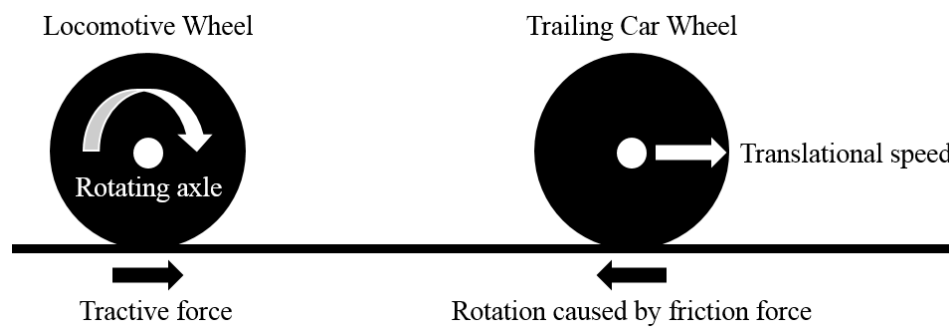
Figure 2.5. Difference in Driving Mechanisms between a Trailing Car and a Locomotive Wheel

In addition to the field experimentation, the mechanical behaviors of a railway track system can also be studied using FE analysis. In a study presented by Nguyen et al. (2011), a 2D and a 3D FE model were both developed to investigate the response of a railway track under high speed vertical dynamic loading. The 2D FE model utilizes Timoshenko beam elements and spring-dampers and allows for significant savings on the computational cost. However, the 2D model lacks the ability to simulate the behaviors of the fastening components for which the 3D FE model is able to compensate. In another study by Chen et al. (2014), a 3D FE model of a track system with detailed fastening components is developed to study the response of the fastening system under combined static vertical and lateral wheel loads. It allows for the investigation of the behaviors of every fastening component. However, the model only considers

static loading scenarios which can compromise the accuracy of the results considering the dynamic effects. As few FE model has been developed for investigating the behaviors of longitudinal force in the railway track system, a 3D dynamic FE model is needed in order to gain insights into this subject.

In addition to the FE model discussed in the previous section, another 3D FE model of a wheel-track system is presented; it focuses on investigating the track response under wheel dynamic longitudinal load. It highlights an 86-foot railway track consisting of detailed 3D fastening components. The extensive length of the track system ensures that little longitudinal force is present in the fastening system at the boundary locations. Field experimental data was also used to validate the FE model. The FE modeling results are then used for the investigation of the behaviors of longitudinal force in the fastening system with different system parameters which include the accelerating rate of the wheel, the elastic modulus of the clips, the COF between the rail and the railpads, and the spacing of the crossties.

CHAPTER 3

FINITE ELEMENT ANALYSIS OF TRACK RESPONSE UNDER WHEEL FLAT INDUCED IMPACT LOADS

3.1. *Finite Element Software ABAQUS*

The commercial finite element software, ABAQUS was utilized in this study. ABAQUS is capable of conducting both static and dynamic simulation and has significant applications typically in a wide range of industries. The software provides both pre-processing and post-processing capabilities. The pre-processing user interface offered the visualization of component and assembly geometry and provided a variety of mesh generation routines (Dassault Systemes Simulia Corp., 2013). As parallelization is allowed, the computational efficiency can be greatly enhanced by taking the advantage of multi-core processors. The software also offers the capability to visualize analysis results, which significantly facilitates the process of post-processing.

In addition to the powerful pre- and post-processing user interfaces, ABAQUS provides capabilities of analysis on a wide range of engineering problems. It is able to conduct basic and advanced linear analysis as well as nonlinear analysis such as the response of structure due to earthquake loading (Dassault Systemes Simulia Corp., 2013). Furthermore, its capabilities are extended to solving multiphysics problems including structural acoustics, thermal-electrical, electromagnetics, and smoothed particle hydrodynamics (Dassault Systemes Simulia Corp., 2013). As the modeled track components can potentially undergo plastic deformation, the nonlinear analysis capability provided in ABAQUS allows for satisfactory prediction of stress-strain behaviors of track components.

Materials of different stress-strain behaviors need to be considered for the modeling of railway track, and thus requires the FE software to integrate sufficient material models. An extensive library of material models is provided by ABAQUS; it can be used to simulate the realistic behavior of traditional engineering materials such as metals and rubber as well as composite and biological materials (Dassault Systemes Simulia Corp., 2013).

As a railway track is a sophisticated system comprising multiple components with a large number of contacting interfaces, the realistic behavior of modeled contact interactions contributes significantly to the validity of numerical solutions. ABAQUS provides comprehensive capabilities in modeling contact interactions, including the ability to model interactions between deformable bodies, rigid bodies, and self-contact. Additionally, ABAQUS allows for automatic detection of contact between different bodies, which dramatically reduces the time required to define contact in complex assemblies such as the railway track system considered in this study (Dassault Systemes Simulia Corp., 2013).

3.2. *FE Model Overview*

In order to gain insight into the effects of impact loads caused by wheel flats on railway tracks, a FE model was developed using ABAQUS. The FE model simulated the rolling of two railcar wheels of an axle, one of which was with a flat spot, on a finite length of a railway track. Figure 3.1 shows the wheels and the cross-section of the track system in the FE model.
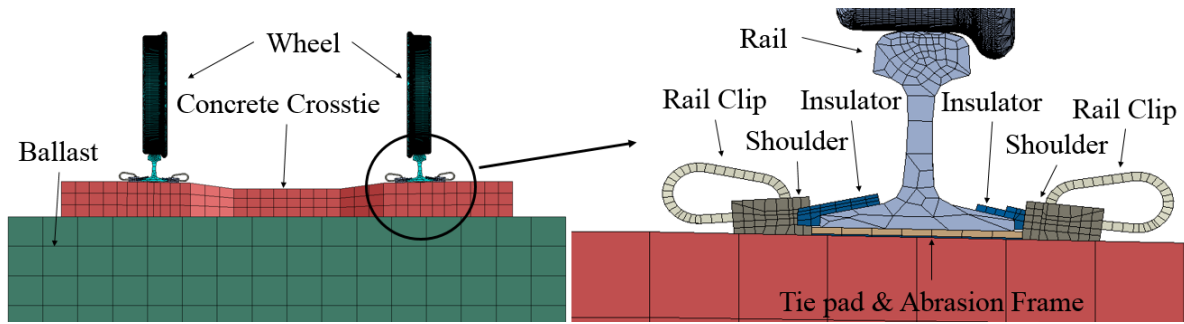
Figure 3.1. Schematic View of the FE Model

The FE model included a tangent track with two railcar wheels, that is, one wheel on each rail. Field experimental results indicated that vertical loadings from the adjacent axles had almost no effect on the track segment under the influence of the flat wheel. In addition, according to Kerr (2003), the distribution of railseat pressure for concrete crosstie track extended less than 7 feet to both sides of wheel load application, which was less than the axle spacing of the passenger coach in the field test. Therefore, incorporating one railcar wheel on each rail was deemed a reasonable assumption. In the modeled track system, 136 RE rails, Safelok I fastening systems and concrete crossties were used. As illustrated in Figure 3.1, the Safelok I fastening system included a rail clip, shoulder, rail pad assembly (i.e. rail pad and abrasion frame), and insulator. The detailed FE model of each track component was described in greater detail in Chen et al. (2014). The wheel was modeled as a narrow flange railcar wheel with 1:40 tapered wheel tread, and the geometries of the wheel web was simplified from curved to flat surfaces. In addition, a rectangular area of flat surface, as shown in Figure 3.2, was created on the tread of one wheel to simulate a wheel flat. The size of the wheel flat, measured tangentially along the wheel perimeter, was specified to be 2 inches. The geometry of track, wheel, and flat spot are consistent with the measurements from field experimentation (details are presented in Section 4.1) for FE model validation.
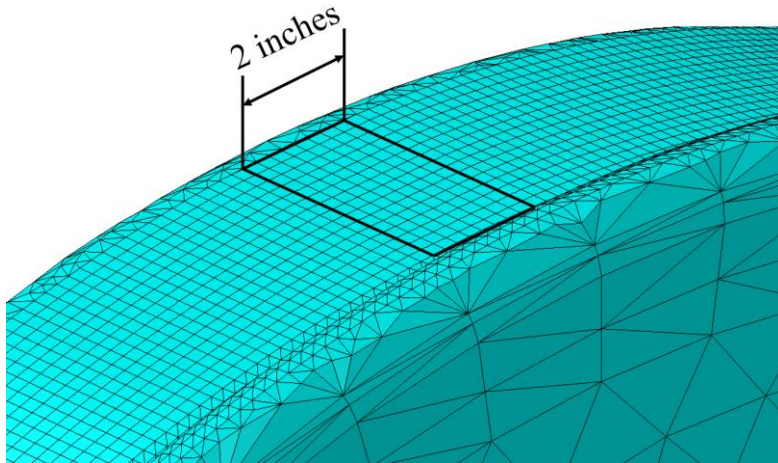
Figure 3.2. Flat Spot on the Wheel Tread

The modeled track system, as shown in Figure 3.3, consisted of 19 sets of crossties and fastening systems with uniform crosstie spacing of 24 inches, summing to 38 feet of track. The track was composed of three parts: a 6-foot segment at the left end, a 14-foot segment at the center, and an 18-foot segment at the right end. The end segments of the track were provided so that, as the impact hit the center of the track, the ends of the rails were not affected by the rail flexural bending under wheel load (Selig & Waters, 1994). In other words, the two end segments served as boundary conditions to the center segment.
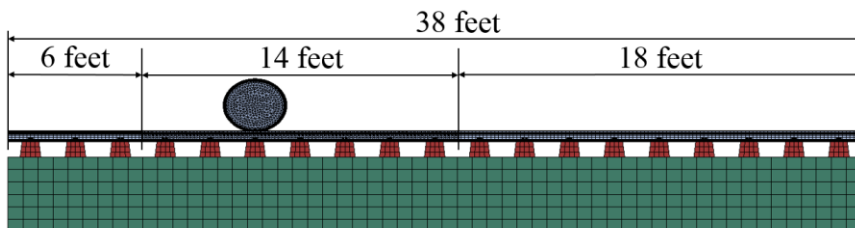
Figure 3.3. FE Model Track Overview (Longitudinal View)

3.3. *Mesh Sensitivity Analysis*

Before element types and sizes were determined, a mesh sensitivity analysis was performed. Mesh densities on track components, except the wheel and rail, were directly referenced from the FE model developed by Chen et al. (2014). Because the mesh density at the contact interface between the wheel and rail has a significantly effect on the accuracy of vertical contact force between the two contact bodies during dynamic simulation, a mesh sensitivity analysis was performed to determine the optimal mesh density on the wheel-rail contact interface. The model was simplified such that only the center segment of rail and wheel were included as the accuracy of interaction force between the wheel and rail was only affected by these two components. The boundary condition was further simplified as the base of rail was fixed. Mesh refinement was only implemented on the perimeter of wheel and the top center of rail to minimize the number of elements and resulting computational time. Convergence was achieved for vertical displacement of the wheel under a static wheel load. Three trials were conducted with three numbers of elements: 21,619, 38,123, and 109,798 (Figure 3.4). It was found that increasing the number of elements by 76.3%, from 21,619 to 38,123, led to an 83.0% decrease in the vertical displacement of wheel. Further increasing the number of elements by 188%, from 38,123 to 109,798, only result in a 32.1% decrease in the vertical displacement of wheel. The results indicated a convergence in the last trial.
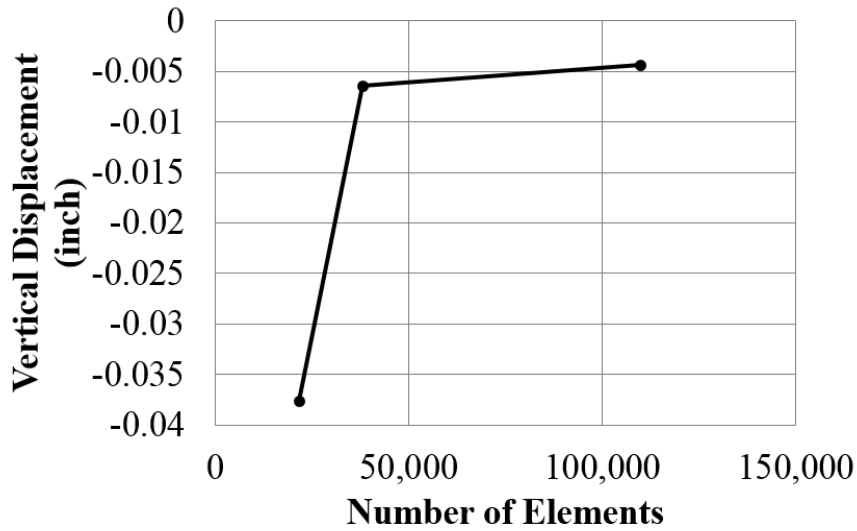
Figure 3.4. Mesh Sensitivity Analysis for Wheel-Rail Contact Interface

With the optimal number of elements on the rail-wheel contact interface determined, the sensitivity of the rail deformation with respect to number of elements was also investigated for vertical strain on the neutral axis of the rail. As the optimal mesh density on the top center of rail was already determined, mesh refinement was only performed on the areas of rail web and base. Figure 3.5 shows the relationship between the vertical strain in the rail and number of elements.
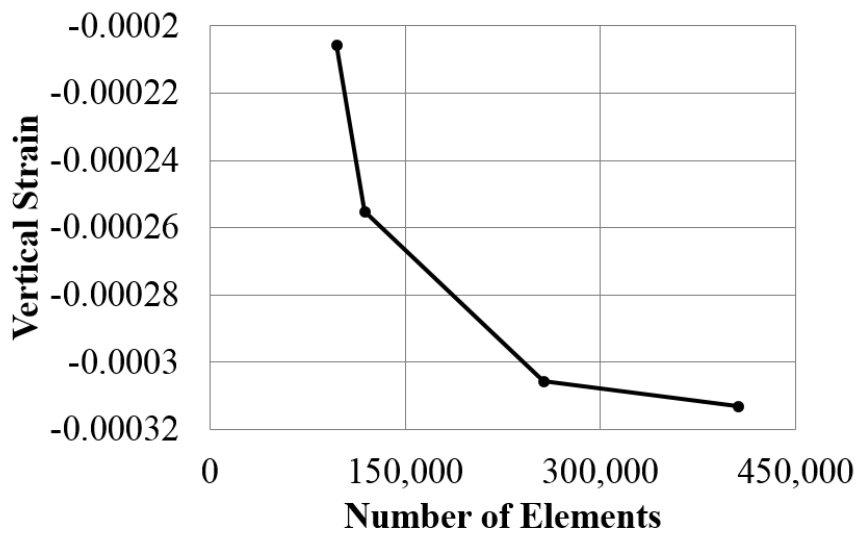
Figure 3.5. Mesh Sensitivity Analysis for Rail Web and Base

Based on the results of mesh sensitivity analysis, extremely refined mesh was required to achieve an accurate numerical solution for wheel-rail contact force. However, as large number of elements from using dense mesh posed considerably higher computational costs, it was only implemented in the 14-foot segment of rail located in the center of track (Figure 3.3). Coarse mesh was implemented on the rail segments at the two ends of track as they were not directly subjected to the wheel load. Figure 3.6 shows the final mesh on the center and end rail segments.

(a)

(b)
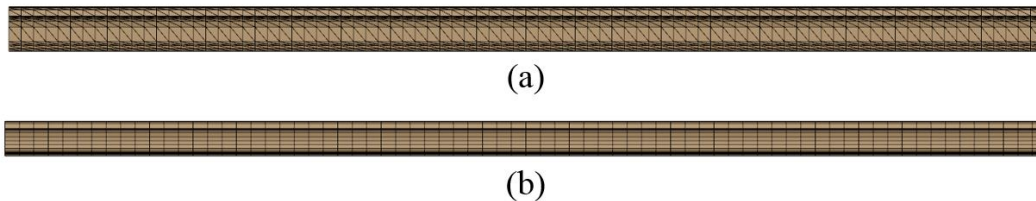
Figure 3.6. Final Mesh on the (a) Center Rail Segment and (b) End Rail Segment

On the center segment of rail, the top center of rail contained the most refined mesh as shown in **Error! Reference source not found.**a and **Error! Reference source not found.**b, and the technique of mesh transition was utilized to ensure smooth transition among elements with different sizes. Similarly, on the wheel, refined mesh was applied on the perimeter of the wheel with transition to coarse mesh in the rest of the body (**Error! Reference source not found.**c).
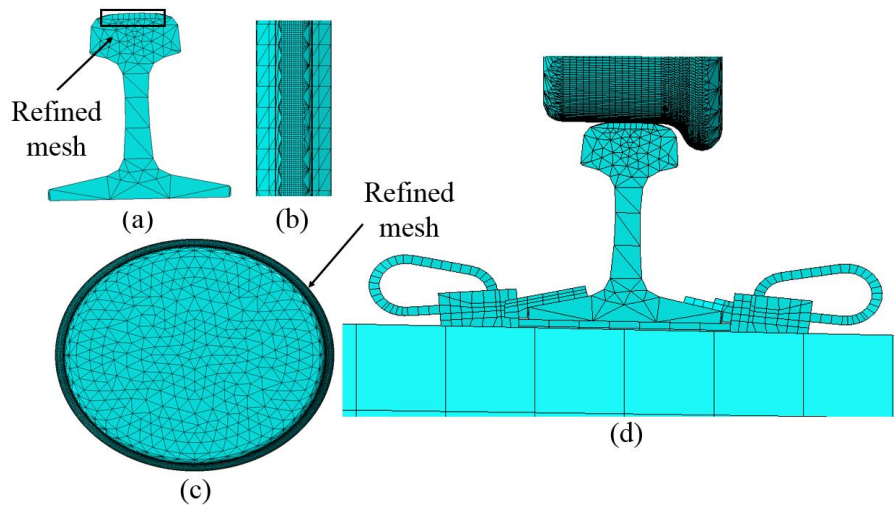
Figure 3.7. (a) Cross-section View of the Center Rail; (b) Top view of the Center Rail; (c) Wheel; (d) Wheel-rail Contact Interface

3.4.   *Element Type and Mesh Size*

All track components were modeled using four-node tetrahedron and eight-node hexahedron 3D deformable solids except for the prestressing strands which were modeled using two-node linear beam elements in the crossties. Because the element size at the contact interface between the wheel and rail is expected to have a significant effect on the accuracy of the output vertical contact force between the two contact bodies during dynamic simulation, refined elements were used on the railhead for the 14-foot rail segment. Elements were used for mesh transition from the refined contact interface to the rest of the rail (**Error! Reference source not found.**). Similarly, refined elements were implemented on the perimeter of the wheel tread with a transition to coarser elements towards the center of the wheel.

3.5.   *Constitutive Relationships*

The material property of concrete was defined using concrete damaged plasticity model that considered two failure mechanisms; tensile cracking and compressive crushing. Under

uniaxial tensile loading, concrete exhibited linear-elastic stress-strain relationship until the

cracking stress was reached, and, thereafter, strain-softening behavior started to take place. An

additional phase, strain-hardening, was present between linear-elastic and strain-softening phases

when concrete was under uniaxial compressive loading. The two damage parameters, d_t and d_c as

shown in Figure 3.8, characterized concrete unloading stiffness and were not defined in the

model as cyclic loading was not included in the model (Chen et al., 2014). The important

variables used to define the constitutive behavior of concrete are summarized in Table 3.1.
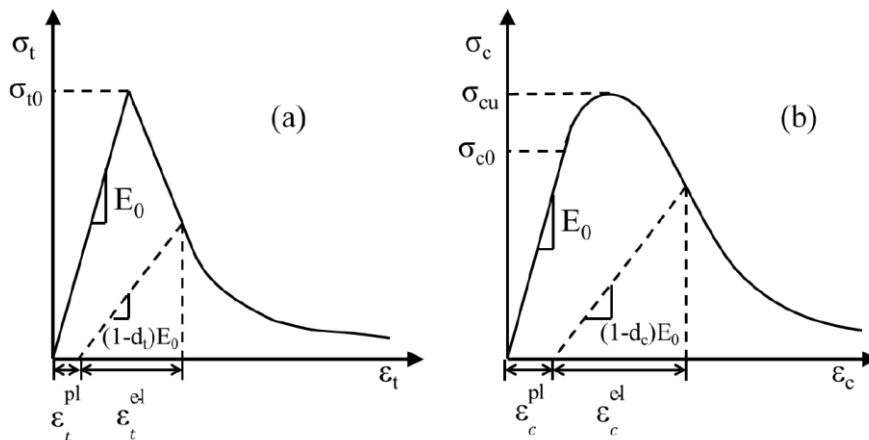
Figure 3.8. Stress-strain Relation of Concrete in (a) Tension and (b) Compression (Dassault
Systemes Simulia Corp., 2013)

In the field, a track substructure is composed of multiple layers that include ballast,

subballast, and subgrade. Given that the substructure is largely made up of discrete particles,

they can be modeled using discrete element method which is able to capture the realistic

response of the track substructure (Huang & Tutumluer, 2011). However, as the computational

cost imposed by discrete element method was high and the focus of this study was not on the

behavior of the track substructure, it was simplified as a single layer of supporting block. The

material property incorporated in the FE model was in accordance with field data obtained from the testing track at TTCI in Pueblo, CO (Grasse, 2013). Based on the measurement results, the hyperelastic material model was defined for the substructure (Figure 3.9). Under compression, the supporting block exhibited a linear stress-strain relation up to a strain value of -0.083%, preceding a nonlinear stress-strain relation thereafter. In the range of nonlinear stress-strain relation, when the stress was increased, the elastic modulus increased as the supporting block hardened.
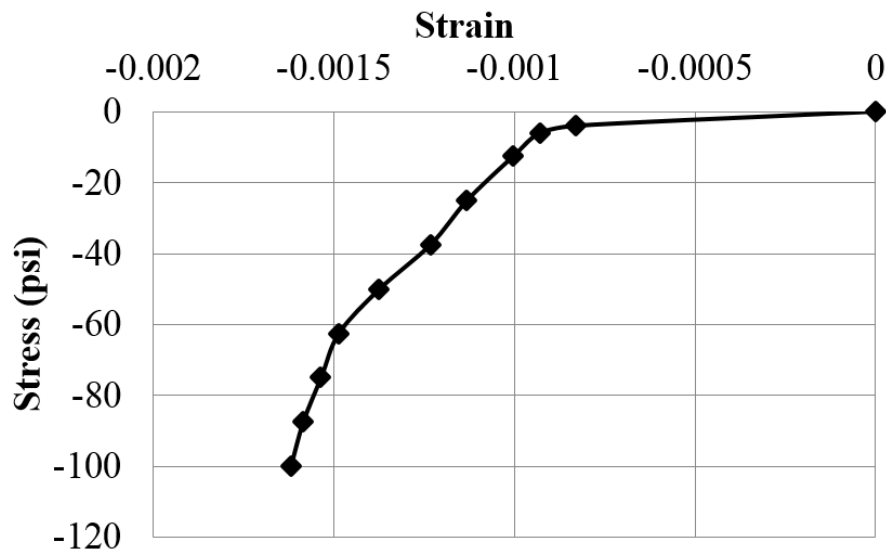
Figure 3.9. Stress and Strain Relation for Track Substructure under Compression

In the FE model, the plastic behavior of rail steel was neglected as the plastic response of the rail was not expected in this research work. Therefore a linear-elastic stress-strain relationship was employed to describe the material behavior of rail. Table 3.1 summarizes major material properties associated with each track component. The field-side insulator is made of two materials; thus it has two material properties listed.

Table 3.1 - Material Properties for Each Track Component

Component	Density (lbs/in^3)	Young's Modulus (psi)	Poisson's Ratio	Yield Strength (psi)	Ultimate Strength (psi)	Ultimate Strain
Abrasion frame	0.0412	4.40E+05	0.35	1.20E+04	N/A	N/A
Ballast	1	N/A	0.4	N/A	N/A	N/A
Clip	0.2836	2.30E+07	0.29	1.83E+05	2.02E+05	0.05
Crosstie	0.08333	4.35E+06	0.2	3.53E+03	7.00E+03	0.00143
Field-side Insulator	0.0412	4.40E+05	0.35	1.20E+04	N/A	N/A
	0.2836	2.45E+07	0.3	4.50E+04	6.50E+04	0.01
Gauge-side Insulator	0.0412	4.40E+05	0.35	1.20E+04	N/A	N/A
Rail	0.29	3.00E+07	0.3	N/A	N/A	N/A
Rail pad	0.0368	7.50E+03	0.394	5.20E+03	N/A	N/A
Shoulder	0.2836	2.45E+07	0.3	4.50E+04	6.50E+04	0.01
Strand	0.29	3.24E+07	0.3	2.55E+05	N/A	N/A
Wheel	0.29	3.00E+07	0.3	N/A	N/A	N/A

3.6. *Contact Interactions*

Contact interactions between track components were formulated using surface-to-surface contact discretization, and a master and a slave surface were defined for each contact pair. This contact formulation method prevents large and undetected penetrations of nodes on master surface into slave surface, providing more accurate stress and strain results compared to other methods (Dassault Systemes Simulia Corp., 2013). The basic Coulomb friction model with the penalty friction formulation was used to simulate the frictional force response at the contact interface. The maximum allowable frictional stress is related to contact pressure by COF between contacting bodies (Dassault Systemes Simulia Corp., 2013). The COFs of the contact pairs in the model were determined from literature (Yamaguchi, 1990; Stachowiak & Batchelor, 2005) and based on a series of large-scale abrasion tests conducted at UIUC (Kernes et al., 2012). Table 3.2 summarizes the values of COFs used in the FE model.

Table 3.2. Coefficient of Friction (COF) Input used in the FE Model

Frictional Interaction	COF
Rail pad-rail interface	0.3
Frame-concrete interface	0.3
Insulator-rail interface	0.15
Insulator-clip interface	0.15
Insulator-shoulder interface	0.15
Shoulder-clip interface	0.5
Crosstie-ballast interface	0.7
Wheel-rail interface	0.0

The wheel-rail contact interaction was simplified from what may occur in reality with either one or two contact patches might present between wheel and rail. The contact patches may include the contact between the wheel tread and rail and/or the contact between the wheel flange and rail (Anderson et al., 2004). However, according to Dukkipati and Dong (1999), wheel-rail friction force has little influence on the impact load. In addition, as the behavior of track system was studied in the vertical plane for this research, the contact between the wheel flange and rail was neglected. Therefore, frictionless contact was defined for the interaction between the wheel and rail.

Contact interaction between the legs of a shoulder and concrete crosstie involves contacts of relatively more complex geometries and was difficult to simulate using conventional contact formulation methods. As the relative movement between the shoulder-insert and concrete crosstie is expected to be negligible, the constraint feature "embedded region" in ABAQUS provides a convenient approach in modeling the interaction. The elements of shoulder inserts were defined to be embedded in concrete crosstie, and the translational degrees of freedom of nodes on shoulder inserts were constrained by that on concrete crosstie, well representing the

bonding between the two components prior to the occurrence of cracking in concrete crosstie (Dassault Systemes Simulia Corp., 2013).

In reality, some amount of bond slippage occurs between prestressing strands and concrete as the concrete crosstie undergoes bending. However, slippage of prestressing strands is not likely to have significant effects on the behavior of fastening components, hence it is neglected for this analysis. Therefore, the "embedded region" constraint that allows no bond-slippage between hosting and embedded regions was used to model the interaction between prestressing strands and concrete crosstie.

No axle was applied in the FE model to connect the two wheels; instead, a reference node was created at the centroid of the wheel to simulate an axle, and the "rigid body" constraint was used to bind the translational and rotational degrees of freedom of all nodes on the wheel with that of the reference node (Dassault Systemes Simulia Corp., 2013). In other words, the rotation and translation of the reference node were transmitted to the wheel.

3.7.   *Loading Procedure and Boundary Conditions*

The FE analysis consisted of two phases. The first phase was the static loading phase that served to stabilize the track system in a static sense before a dynamic simulation. The static analysis phase included prestressing concrete crossties with strands, clamping clips onto the rail, applying gravity loads to the system, and applying the wheel load. Following the manufacturer's specification, the tensile capacity of all the prestressing strands was 8.75 kips/strand. A prestressing force of 7 kips was applied to each of the 20 strands embedded in each concrete crosstie, which was 80% of the tensile strength of a strand. When the prestressing force was released, the deformation of strands would engage concrete with compressive force. In the FE model, the assembly of clips was initiated in the same step. Pressures were first applied to lift up

30

the toes of clips over the insulators. With the pressures applied, clips were then displaced towards the rail and the clip inserts were socketed into the grooves on the shoulders. As the tips of clips were directly placed over insulators, lifting pressure was decreased and the clips, then, clamped onto the insulators. The following step was to apply gravity loads to the superstructure components of the track system to simulate the resistance to upward deflection resulted from the vertical wheel load. In addition, the wheel load was applied to the reference point of the wheel. Figure 3.10 illustrates the loading and boundary conditions in each step.

The next phase was the dynamic simulation as shown in Figure 3.10, Steps 7 – 9. ABAQUS provides two types of integration schemes for dynamic simulation: explicit and implicit time integration schemes. An explicit dynamic analysis is computationally efficient for analyzing large models with relatively short dynamic response times and for analyzing events or processes that are extremely discontinuous. It takes small time increments and is typically chosen for transient time dynamic analysis. In contrast, an implicit dynamic analysis usually gives acceptable and/or more stable solutions with time increments typically larger than explicit schemes by one to two orders of magnitude (Dassault Systemes Simulia Corp., 2013). As the total dynamic step running time was expected to be relatively long, explicit schemes are less computationally efficient. Therefore, implicit schemes were selected for the dynamic simulation. The increment time around time of impact was refined such that the transient effects could be simulated accurately. In the three dynamic analysis steps, a rotational speed and a translational speed were both applied to the reference nodes at the center of the wheels. The total dynamic simulation time was deemed sufficient as the wheel-rail interaction force could reach dynamical equilibrium prior to impact and the wheel could keep rolling some distance after the impact.
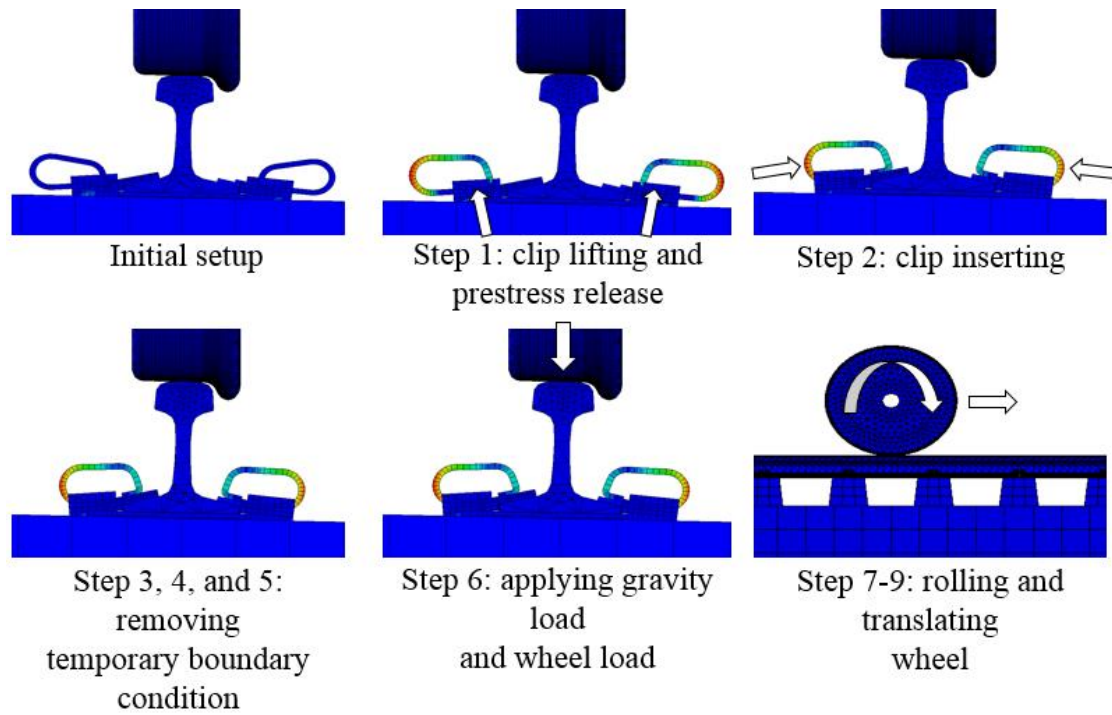
Figure 3.10. Sequence of Application of Loadings and Boundary Conditions in the FE Model

CHAPTER 4

FINITE ELEMENT MODEL VALIDATION FOR IMPACT LOAD MODEL

4.1.   Field Test Setup

Field experiments were conducted by researchers of University of Illinois Rail Transportation and Engineering Center (RailTEC) at the Transportation Technology Center, Inc. (TTCI) in Pueblo, CO, USA. The results from the testing on a tangent track section were used for model validation. For this segment, 15 new concrete crossties were installed and tamped prior to experimentation, and strain gauges were installed on the rail to record the dynamic wheel loads and rail behavior (Figure 4.1).

Figure 4.1. The Instrumented Track Segment at TTCI

To quantify the actual vertical wheel loads entering the rail head, strain gauges were installed on both sides of rail web. As shown in Figure 4.2, Chevron patterns which consisted of two gauges placed perpendicular to each other were installed 6 inches apart and centered in the crib (the portion between two crossties) at the rail's neutral axis on both sides of rail.
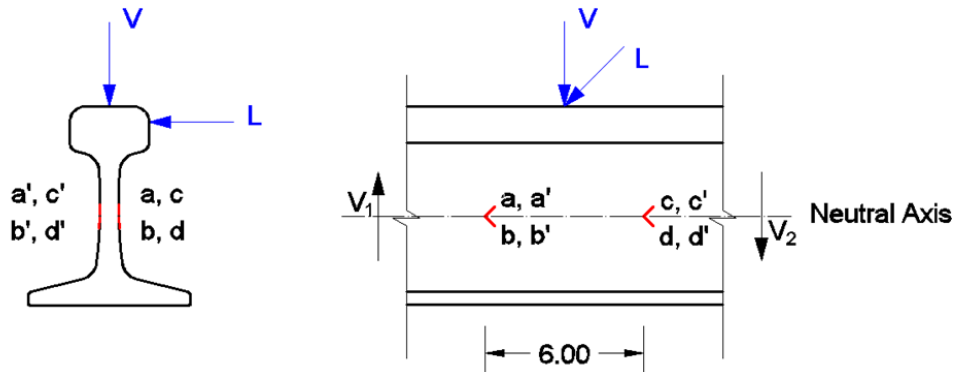
Figure 4.2. Strain Gauge Pattern for Vertical Wheel Load Measurement

By wiring strain gauges into a Wheatstone bridge, the difference of the averaged shear strain at the left and right side of the applied load can be output. Referring to Euler-Bernoulli beam theory, the concentrated applied load can be calculated by combining the shear deformation with the cross-sectional properties of the rail. For accuracy, the strain gauge bridges were calibrated under static loads prior to the dynamic testing.

Strain gauges were also installed in the vertical direction above the railseats to examine the rail behavior under the wheel loads (Figure 4.3). For the instrumented locations, three gauges were placed in a line on both sides of the rail. To eliminate the effect of lateral wheel loads, the average value measured from the front and back sides of rail was used to compare with the modeling results.
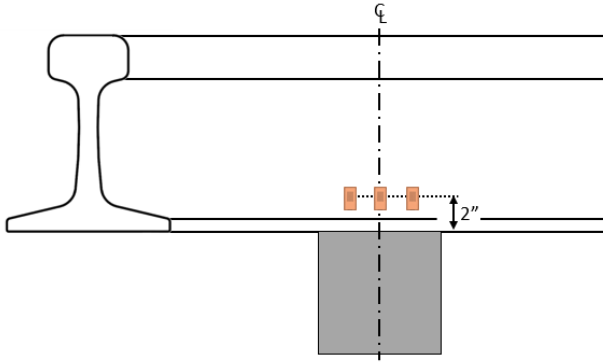
Figure 4.3. Locations of Vertical Strain Gauges Placed Above Railseat

4.2. *Field Validation of FE Model with No Impact Load*

Component–level models and single-crosstie FE models were previously calibrated with

field and laboratory experimental results (Chen et al., 2014). Therefore, only system level

validation was performed for this FE model. The FE model was first validated with the absence

of an impact load; two recorded time histories were compared with the FE model: vertical strains

in the rail web and vertical internal strains of the concrete crosstie read from embedment strain

gauges.

The validation based on the vertical strains in the rail web ensured that the vertical

reaction forces transmitted from the wheel to the rail was physically making sense. Figure 4.4

presents the comparisons between the field and numerical results. A section of signal containing

eight peaks is shown, in which the first two peaks are caused by the last two axles of a car, the

middle four peaks are due to all the four axles of the car following, and the last two peaks are

from the first two axles of the third car. Due to the rail roughness and other geometry

imperfections, slight fluctuation was observed in the field data. Because of the limitation of the

length of the track in the finite element model, short during of signal was recorded. To make an

appropriate comparison, the peak of finite element output is aligned to the first peak of the field

data. Comparing the output from the finite element model with the field data, the shapes of the two curves exhibited good agreement. Both curves show that the vertical strain in the rail web decreases first and reaches a minimum value (maximum compression), then starts to increase after the wheel passage. The FE model gave a maximum compressive strain value of 150 micro strain which was 4.7% higher than the 143 micro strain measured in the field. Although the upper half of the signal from the finite element result looks like narrower than that from the field test, it could be explained by the fact that only one axle was modeled in the finite element analysis, which neglected the affect from the adjacent axles. Therefore, a good agreement between field and numerical results for vertical strain in rail web was achieved.
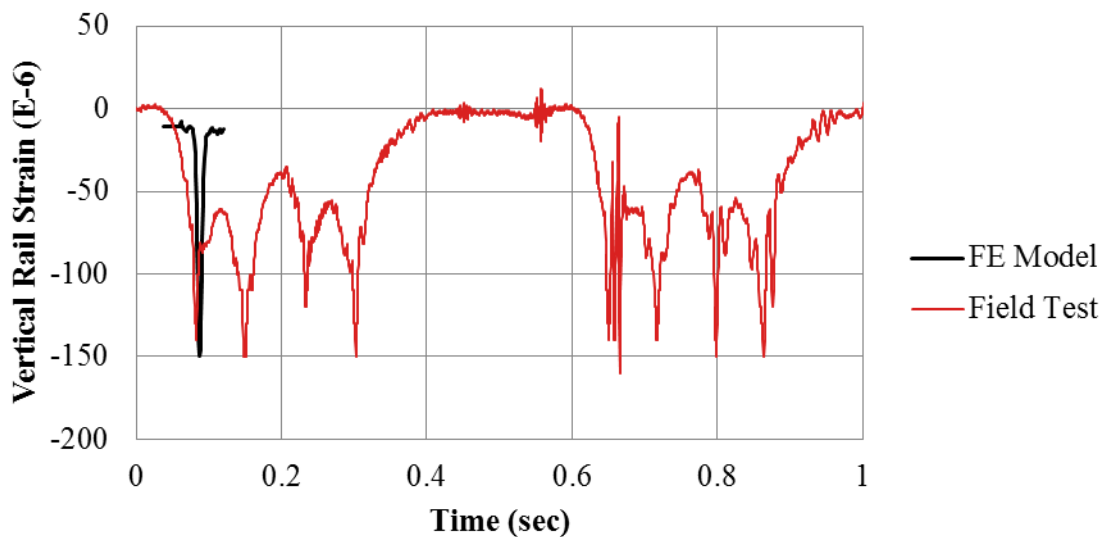
Figure 4.4. Vertical Strain in Rail Web with no Impact Load

In addition to the vertical strain in the rail web, longitudinal strain measured 2 inches below the surface of the concrete crosstie at the railseat was also calibrated against field data. Figure 4.5 illustrates the comparisons between the field results and the numerical solutions. Similar to Figure 4.4, the finite element signal was aligned with the first peak of the field data.

36

Despite the fluctuation in the field data caused by imperfect field conditions, the curves exhibited similar trend. A maximum compressive strain was observed during the passage of a wheel, indicating the measurement area was subjected to compression. The maximum compressive strain value measured from the field was 84 micro strain and was 5.2% higher than the numerical solution, hence good agreement was shown.
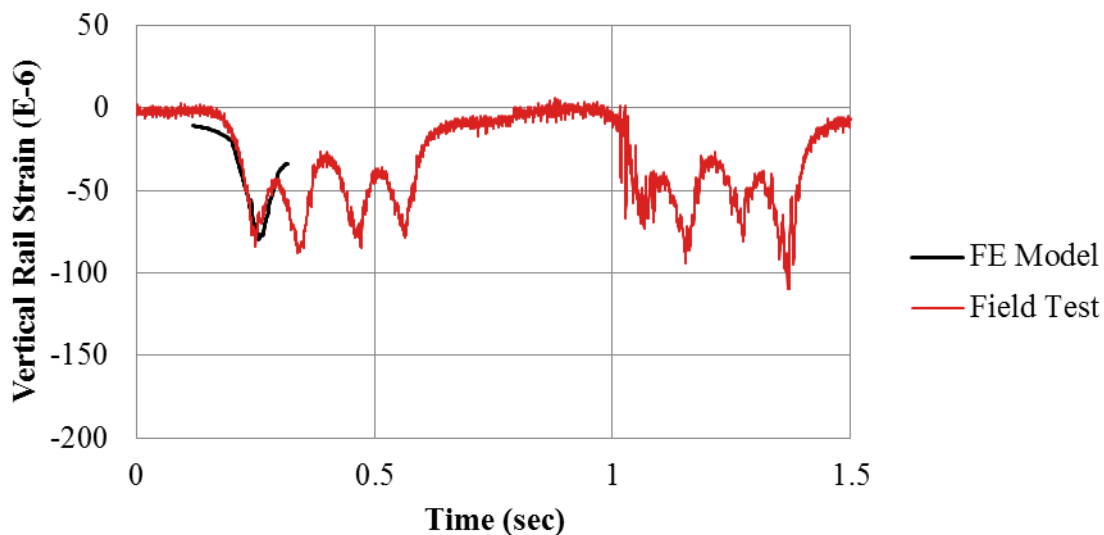
Figure 4.5. Embedment Strain in Concrete Crosstie with no Impact Load

4.3. *Field Validation of FE Model with Impact Load*

4.3.1. *Impact Force*

In the field experimentation, a wheel with a flat spot on its tread was placed on the third axle of the 9th car of the freight consist. The diameter of the flat spot was measured as approximately 2 inches (Figure 4.6). For the FE model validation, the train speeds in the field experimentation and FE model were both 45 mph.
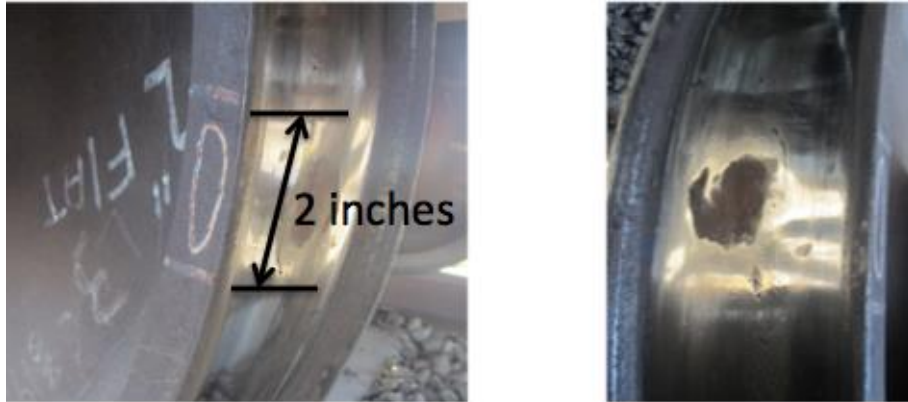
Figure 4.6. Flat Spot on the Wheel

The dynamic wheel loads as well as the impact loads due to train passage were measured with the strain gauge bridges (Figure 4.2). Figure 4.7 presents the time history of the four axles of the 9th car rolling over the instrumented track section. It should be noted that the calibration of the bridges were conducted under various static loads applied immediately above the center of two Chevron patterns. Therefore, the history of the measured vertical wheel loads is only valid at the center point of each peak. In Figure 4.7, the measured dynamic vertical loads due to the second, third and fourth wheel are all about 34 kips. Due to the existence of the flat spot located at the first wheel, the first peak in Figure 4.7 splits up into two much narrower peaks, which exceed the magnitude of the other readings by a factor of two. The separated peaks could be explained by the vibrations of rail and wheel aroused by the large impact load caused by the flat pattern.
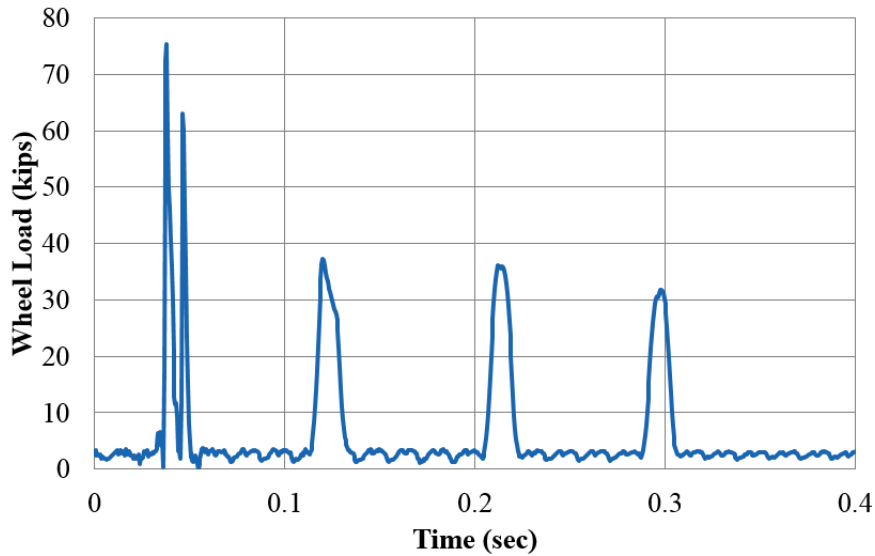
Figure 4.7. Time History of the Vertical Loading Output from a Strain Gauge Bridge

For comparison, in the FE model, three cases of impact loading caused by the flat spot were examined: the flat spot hitting directly above the centerline of a railseat, 2 inches before approaching the railseat, and immediately above the centerline of a crib. The monitored wheel load history for the three cases is shown in Figure 4.8. Because Figure 4.8 presents the actual wheel-rail contact force output from the model directly, it shouldn't be used to compare with the shape shown in Figure 4.7. From the wheel load history, it could be found, regardless of the flat spot hitting location, the shape of the impact load is very similar. The magnitude of the impact load recorded from the model is approximately 74 kips, which is about 1% lower than the peak of the impact load measured from the field. In addition, split peaks were also observed in the numerical results, which confirmed the vibration of the rail and wheel as a result of the impact.
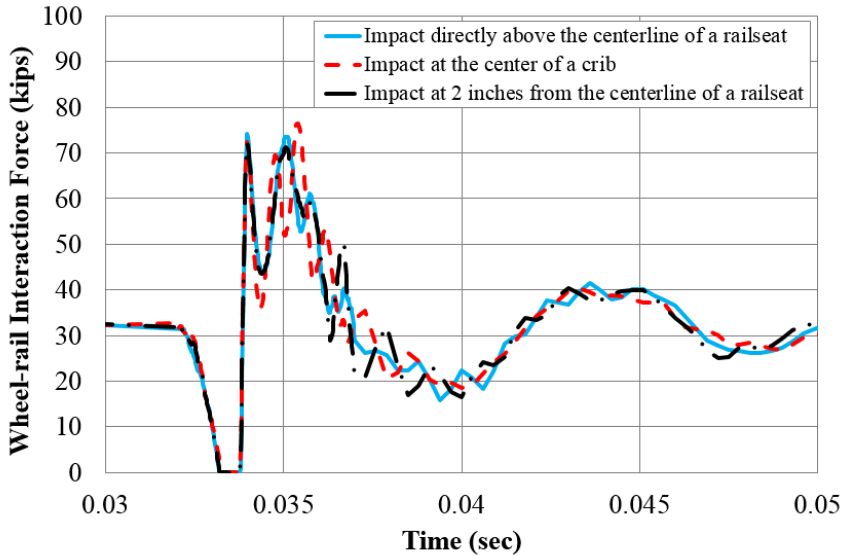
Figure 4.8. Wheel Load History Output from FE Model

In all three cases, the interaction force exhibited an abrupt decrease to zero prior to the

occurrence of wheel impact, which indicated a loss of contact between the wheel and the rail. As

illustrated in Figure 4.9, this observation can be attributed to the sudden change of contact from

the intact wheel tread to a flat spot, which causes the wheel to lose contact with the rail for a

transient time. In addition, the impact loadings were superimposed by multiple peak loads which

were caused by different mechanisms. The first peak load was a result of the colliding of wheel

and rail as shown in Figure 4.9, hence referred to as the direct impact load. The peak loads that

followed were from the vibrations of the track system under the influence of wheel impact, and

thus were the vibration-induced impact loads.

40
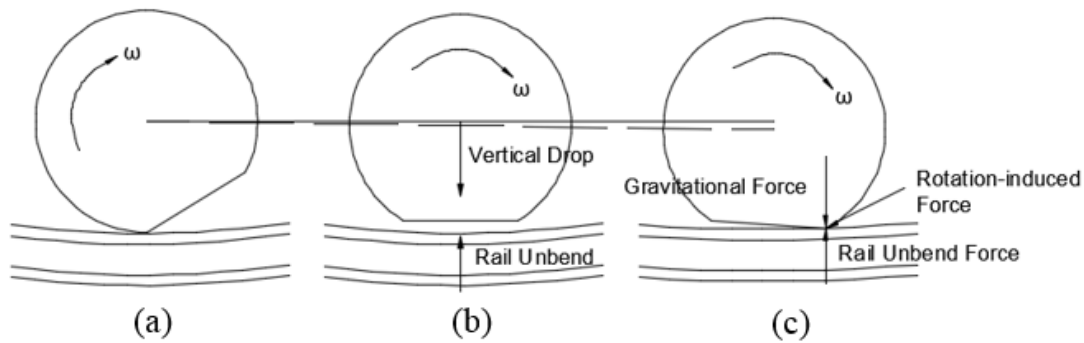
Figure 4.9. Changes of Wheel-rail Contact with a Flat Wheel

As shown in Figure 4.8, the magnitudes of impact loading were similar and not significantly affected by the location of impact. When the impact occurred directly above the centerline of the railseat, the impact loading was 74 kips, which slightly increased to 77 kips when the location of impact was above the centerline of the crib. In addition, an impact loading of 72 kips was observed as impact location was moved 2 inches away from the railseat. However, a considerable difference was observed for the patterns of wheel-rail interaction force. In the case where the impact occurred at the center of a crib, the fluctuations of loading history were found to be stronger, indicating a larger extent of vibrations in the track system. In addition, the maximum impact load was the vibration-induced load as opposed to the other two cases in which the direct impact load was larger. It indicates that loads caused by the vibrations of the track system have a potential to surpass the loads produced by the impact of the wheel on the rail, and therefore, both the direct impact load and vibration-induced impact load need to be attenuated in order to mitigate the damage from impact loadings.

4.3.2. Vertical Strain in the Rail

Vertical rail strains were also used to validate the FE model. In the same manner used for wheel load validation, the flat spot hit the rail at three locations in the FE model. Figure 4.10 – Figure 4.12 present the comparison of the field and numerical results under these three loading conditions. It has been validated that the maximum vertical rail strain due to round wheel is about 150 micro strain in compression (Figure 4.2). When the flat wheel hit immediately above the centerline of railseat (Figure 4.10), due to the superposition of regular wheel load and impact, the magnitude of strain was raised up to about 170 micro strain in compression. This was demonstrated by both FE and field testing results. Similar to the wheel load, split peaks were found, followed by smaller fluctuations. When the flat spot hit 2 inches ahead of the railseat (Figure 4.11), the magnitude of the first peak was decreased, followed with a high peak with a magnitude of about 150 micro strain in compression. The reduction in strain following the first peak could be explained by the short duration of disengagement of wheel and rail when the flat spot rolled directly above the rail, which has weakened the effect of wheel load. The second peak was due to the re-engagement of the wheel and rail which could be seen as the source of the impact. When the flat spot hit the center of the crib beyond the location of strain measurement (Figure 4.12), a secondary peak was recorded next to the main peak due to the round wheel. Because the impact occurred 2 inches away from the strain measurement, its influence was not as strong as the first and second cases. The maximum strain due to the impact corresponding to the third case was found to be 75 micro strain in compression.

42
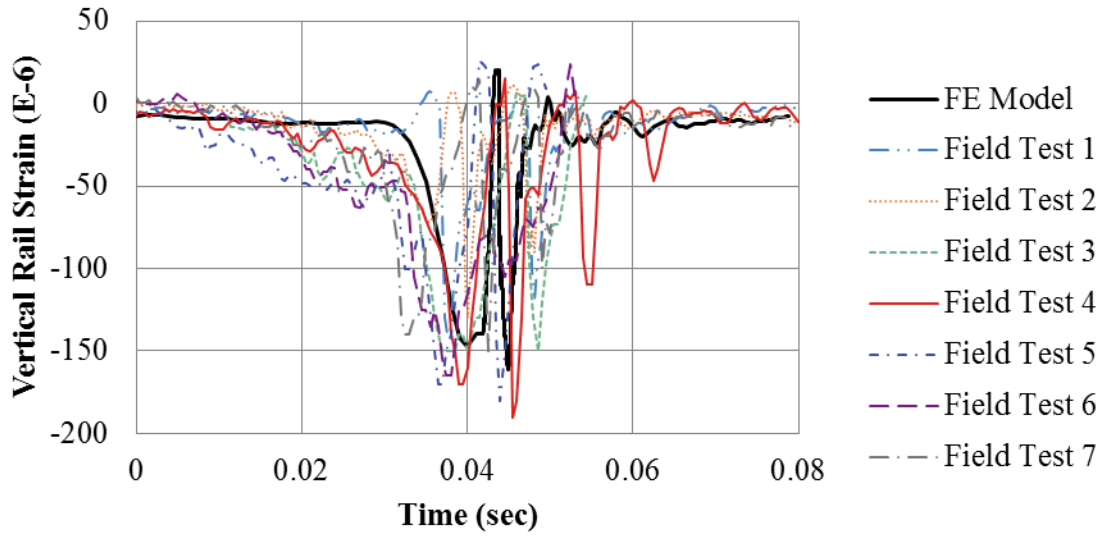
Figure 4.10. Vertical Rail Strain due to Flat Spot Hit Directly Above the Centerline of Railseat
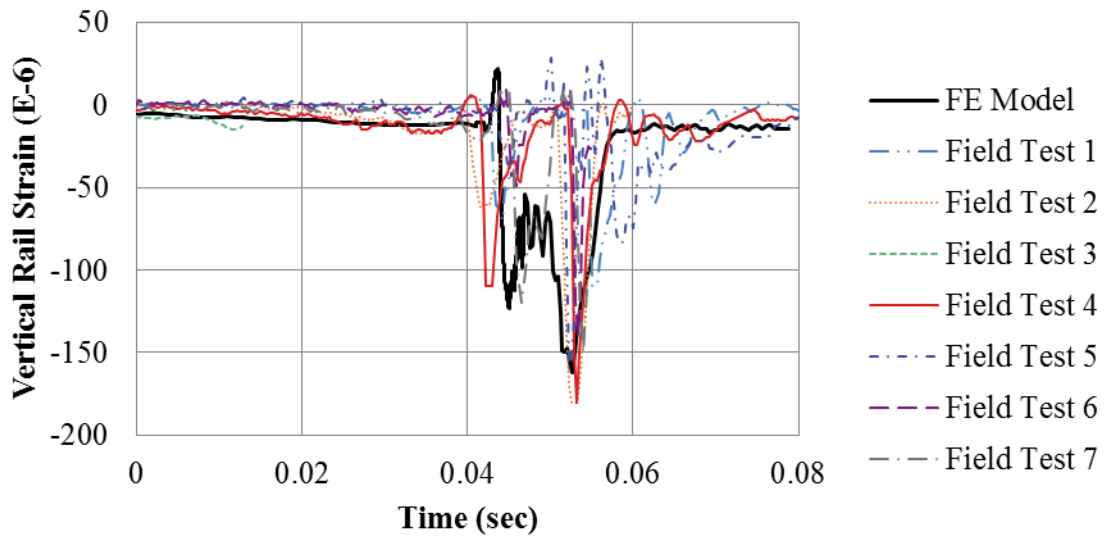
Figure 4.11. Vertical Rail Strain due to Flat Spot Hit 2 inches Ahead of the Centerline of Railseat
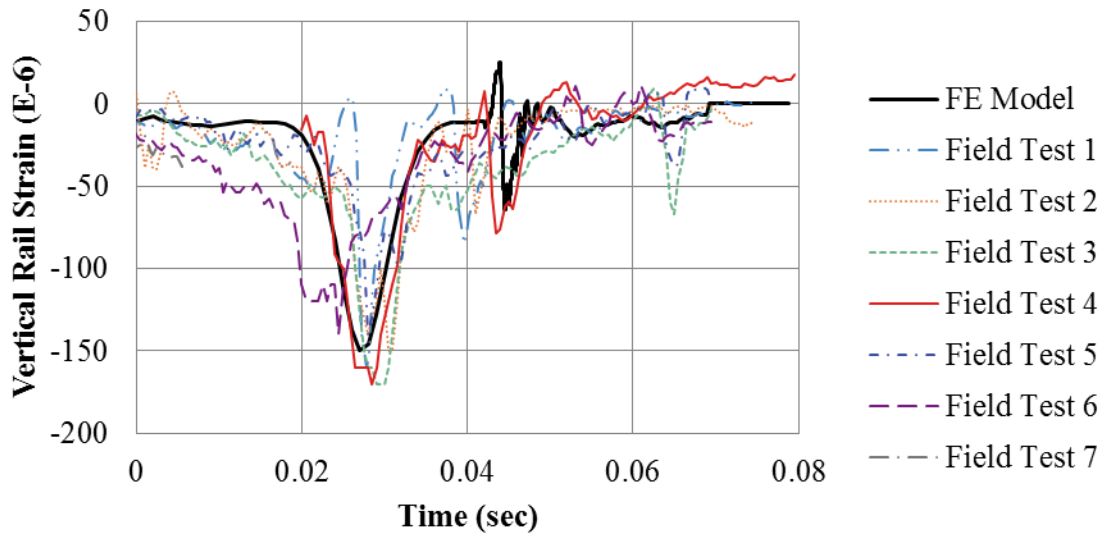
Figure 4.12. Vertical Rail Strain due to Flat Spot Hit Directly Above the Centerline of Rail Crib

CHAPTER 5

FINITE ELEMENT ANALYSIS OF TRACK RESPONSE UNDER

LONGITUDINAL LOADS

5.1.   FE Model Overview

In order to gain insight into the behavior of the fastening system under dynamic

longitudinal wheel load, another FE model was developed also using ABAQUS (Dassault

Systemes Simulia Corp., 2013). The FE model simulated the rolling of a locomotive wheel on a

finite length of a railway track. As mentioned in Section 2.4, the maximum longitudinal wheel

load is imparted from an accelerating locomotive wheel, thus the FE model only considered a

locomotive wheel. Figure 5.1 shows the wheel and the cross-section of the track system in the FE
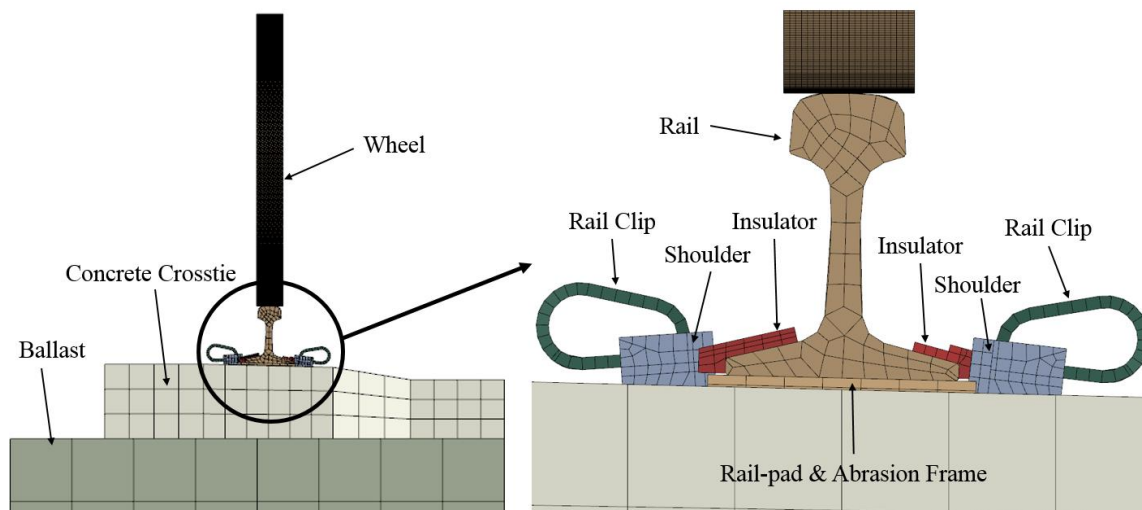
model.

Figure 5.1. Schematic View of the FE Model

The FE model included a tangent track with a locomotive wheel. As the tangent railway track was symmetric about its center, the FE model only concerned half of the track system, which significantly reduced the computational cost. The wheel-rail contact interaction was simplified from what may occur in reality where either one or two contact patches might present between wheel and rail. The contact patches may include the contact between the wheel tread and rail and/or the contact between the wheel flange and rail (Anderson et al., 2004). However, the wheel flange and rail contact was assumed to have little effect on track longitudinal response, thus the wheel is modified such that the flange was neglected compared to the FE model discussed in Chapter 3. As illustrated in Figure 5.1, the wheel was modeled with a circular plate which represented the wheel tread and web. In addition, same track components were included in the FE model.

Compared to the other FE model (Section 3.2), the length of track was extended as shown in Figure 5.2. The modeled track consisted of 43 sets of crossties and fastening systems also with uniform crosstie spacing of 24 inches, summing to 86 feet of track. The track was also composed of three parts: a 36-foot segment at the left end, a 14-foot segment at the center, and another 36-foot segment the right end. The length of the center segment was the same as the other FE model whereas the end segments were lengthened. As the rail is much stiffer longitudinally than vertically, longitudinal force remains more significant than vertical force beyond the region affected by vertical wheel loads (Rhodes & Coats, 2008). Therefore, the extended length of the end segments allowed for the fastening system located at the boundaries to experience little longitudinal force.
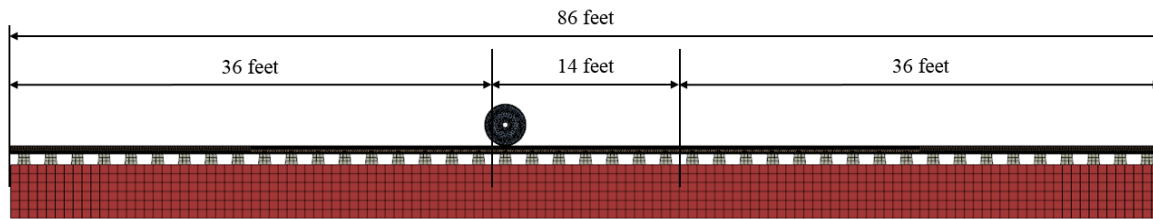
Figure 5.2. FE Model Track Overview (Longitudinal View)

The components in the FE model used the same types of elements and mesh as that presented in Section 3.4. In addition, same materials properties were also applied for the track components as summarized in Table 3.1.

Same COFs were used for contact pairs as discussed in Section 3.6 except for the interaction between the wheel and rail. Frictionless contact interaction was assumed in the other FE model (Section 3.6) as the effect of wheel-rail friction was considered insignificant on the behavior of impact load. On the contrary, as the frictional interaction between the wheel and rail was the cause of longitudinal force imparted in the rail, the assumption could no longer hold reasonable. The COF between the wheel and rail is a variable with high degree of nonlinearity and is dependent on a variety of field variables, including temperature, humidity, speed, etc. Based on the findings of an experimental study on the adhesion behavior between wheel and rail, the COF ranges from 0.4 to 0.5 under dry conditions; and the value decreases with increasing speed (Wang et al., 2011). As a simplification, a COF of 0.5 between the wheel and rail was used in the FE model.

5.2.   *Loading Procedure and Boundary Conditions*

The FE analysis consisted of two phases. The first phase was the static loading phase which was the same as the static loading phase discussed in Section 3.7. The detailed sequence of application of loading and boundary conditions is shown in Figure 5.3. The dynamic simulation followed the static loading phase. As the implicit time integration schemes allowed for larger increments of time than explicit schemes and the total dynamic step running time was expected to be relatively long, the dynamic simulation step again utilized the implicit schemes. To conform to the acceleration of the passenger train in the field experimentation, a rotational acceleration of 0.65 radians/sec^2, equivalent to a translational acceleration of 4.81 inch/sec^2, was applied to the reference node at the center of the wheel in the dynamic simulation step in the FE model. The total step time was deemed sufficiently long for the wheel to pass the center segment of rail such that enough data points could be collected.

Initial setup	Step 1: clip lifting and prestress release	Step 2: clip inserting
Step 3, 4, and 5: removing temporary boundary condition	Step 6: applying gravity load and wheel load	Step 7: accelerating wheel
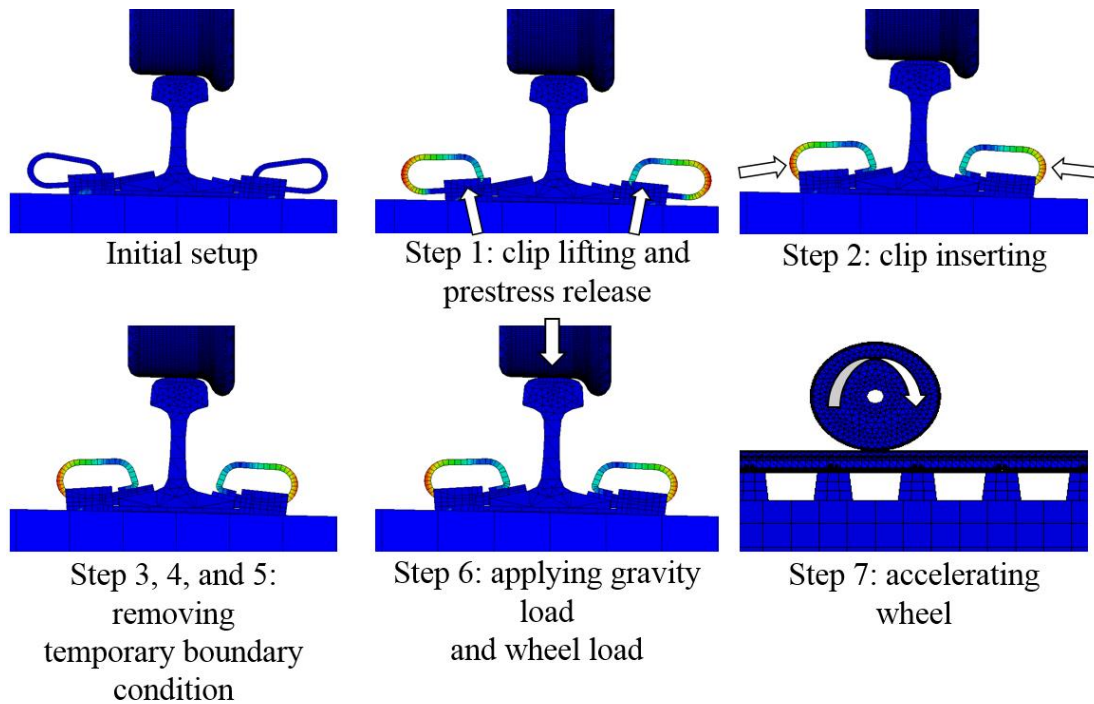
Figure 5.3. Sequence of Application of Loadings and Boundary Conditions in the FE Model

48

CHAPTER 6

FINITE ELEMENT MODEL VALIDATION OF LONGITUDINAL LOAD MODEL

6.1. *Field Test Setup*

Field experimentation data was obtained from the same field experiments conducted at TTCI in Pueblo, CO, USA (Section 4.1). In addition to the vertical strain gauges that were already discussed, strain gauges were also installed on the rail web to measure the longitudinal strain in the rail under the passage of the testing train. The layout of the longitudinal strain gauges also formed chevron patterns except that the two perpendicular strain gauges were aligned vertically and longitudinally. And the strain gauges were installed on the neutral axis of the rail and at the center of the crib.

In addition, linear potentiometers were installed to measure the longitudinal displacement of railpad under the influence of longitudinal wheel loads. Figure 6.1 shows the location of the linear potentiometer; it was placed at the edge of the crosstie such that the tip of it was in contact with the railpad. Readings recorded from the linear potentiometer that had positive values indicated that the railpad displaced along the same direction the train was traveling and vice versa.
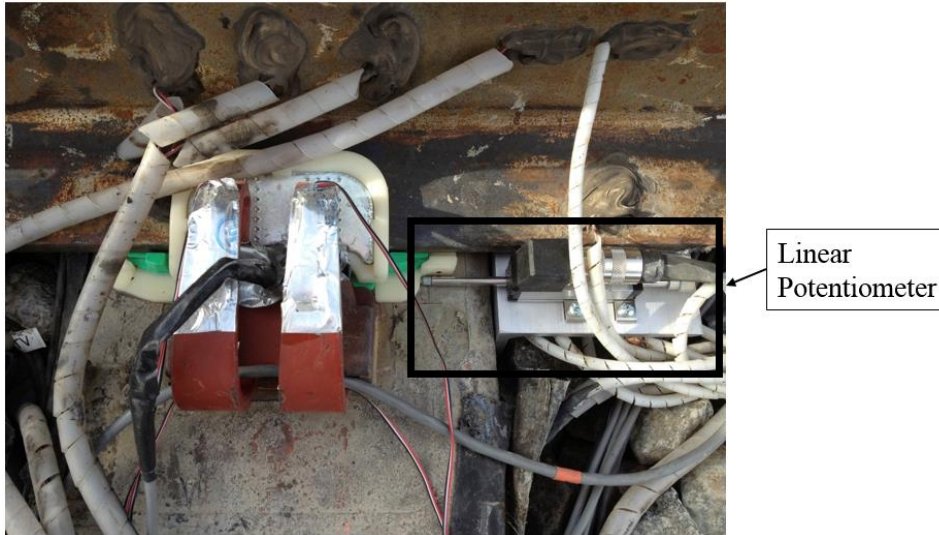
Figure 6.1. Linear Potentiometer Placement in the Field Experimentation

6.2. *Testing Train Consists*

The field experimentation was conducted using two types of trains: a passenger train and a freight train. The passenger train consisted of an EMD four-axle unit and nine four-axle passenger coaches. The locomotive weighed 259.6 kips, resulting in an average wheel load of 32.45 kips. The weight of each passenger coach was approximately 87 kips. The freight train consisted of the same locomotive and 10 four-axle freight cars. Except for an empty car that weighed 44 kips, each three of the rest nine cars had the same weights; and the three different weights were 263, 286, and 315 kips. The arrangements of cars and their weight correspondence are shown in details in Figure 6.2.
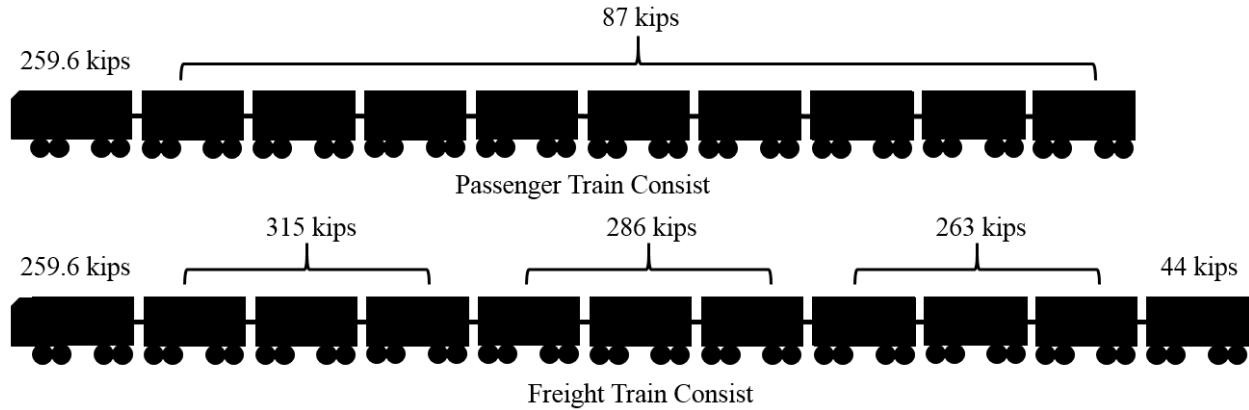
Figure 6.2. Car Weights of Passenger and Freight Train Consists

As aforementioned, a locomotive wheel was expected to produce much higher longitudinal load than a railcar wheel. Therefore, in order to validate the FE model, data recorded during the passage of locomotive wheels was used.

6.3.   *Field Validation of FE Model*

As component–level models and single-crosstie FE models were previously calibrated by Chen et al. (2014), validation was again only performed on the system level for this FE model. The FE model was validated by comparing recorded time histories of three properties: vertical and longitudinal strains in the rail and longitudinal displacement of the railpad. The validation based on the vertical and longitudinal strains of the rail web ensured that the vertical and longitudinal forces transmitted from the wheel to the rail were physically making sense. And validating the longitudinal displacement of the railpad in the FE model assured the longitudinal force transferred from the rail to the railpad was a close approximation of the field condition.

In the FE model, the wheel accelerated from stationary; while, in the field experimentation, the train accelerated past the instrumented section with some initial speed. In other words, the testing data and the modeling data had different time scales. Therefore, side-by-

side comparisons were made and the emphasis was on the peak values observed and the shapes of the curves.

6.3.1. *Longitudinal Displacement of the Railpad*

Based on field and numerical results (Figure 6.3), the railpad underwent a positive displacement followed by a negative displacement. As the rail and railpad were in contact, the moving direction of railpad always conformed to that of the rail. Therefore, the positive displacement was attributed to the positive longitudinal elongation of rail as a result of Poisson's effect under the influence of vertical wheel load as the wheel approaches (Figure 6.4). Similarly, the negative displacement was a result of both the negative longitudinal elongation of rail, as illustrated in Figure 6.4, and movement of rail along the negative direction due to wheel-induced friction force. As shown in Figure 6.3, the shape of the modeling data well resembled the field data. Field data showed a maximum positive displacement of 0.000922 inch compared to 0.000867 inch from the numerical result, resulting in a mere 5.96% difference. The maximum negative displacement in the FE model was -0.000421 inch and was 8.45% less than the field data of -0.00046 inch. The percentage differences were considerably small; therefore, a good agreement between the field and modeling data was realized for the longitudinal displacement of the railpad.
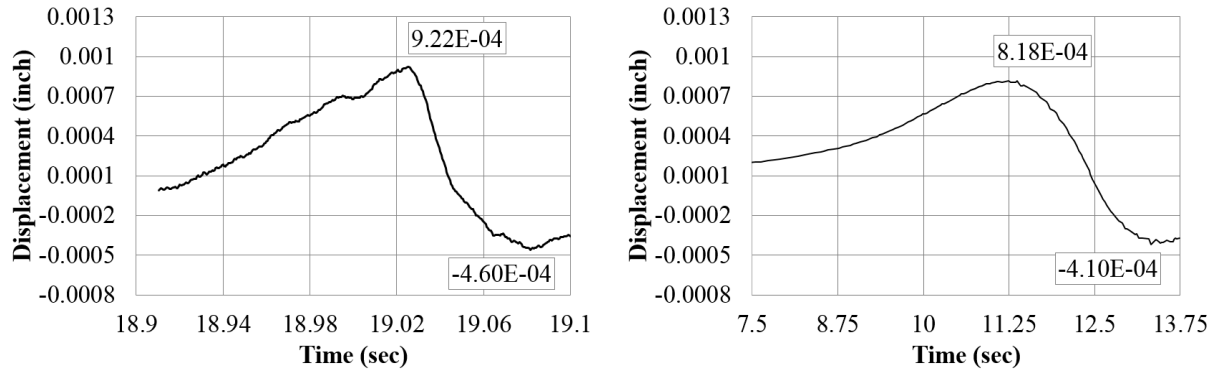
Figure 6.3. Comparison between Field Data (left) and Modeling Data (right) for Railpad Longitudinal Displacement
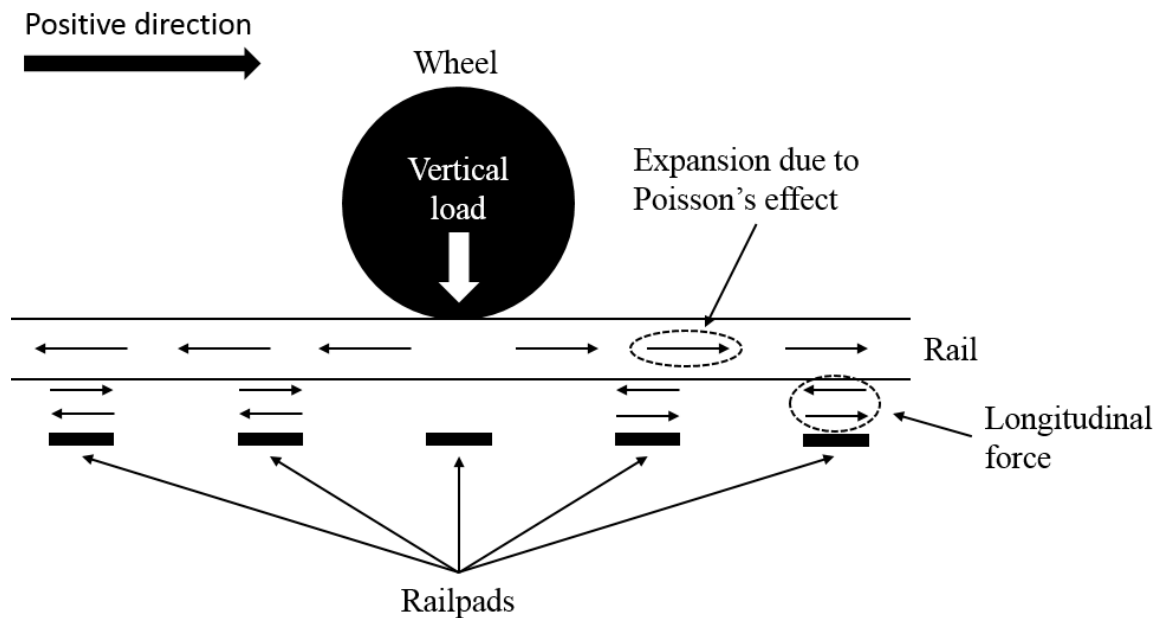
Figure 6.4. Longitudinal Force at the Rail-railpad Interface due to Vertical Wheel Load

6.3.2. *Longitudinal Strain in the Rail*

Figure 6.5 shows the comparison between the field data and numerical data for the longitudinal strain in the rail. In both curves, a minimum value (maximum compression) was proceeded and followed by two positive peak values (maximum tension). The field data gave a

53

maximum compressive strain value that was 6.23% greater than the numerical result. In addition, the FE model gave two maximum tensile strain values that were 20.5% and 13.5% less than the field data, respectively. Therefore, a considerably good comparison was observed between the field data and the numerical result for the longitudinal strain in the rail.
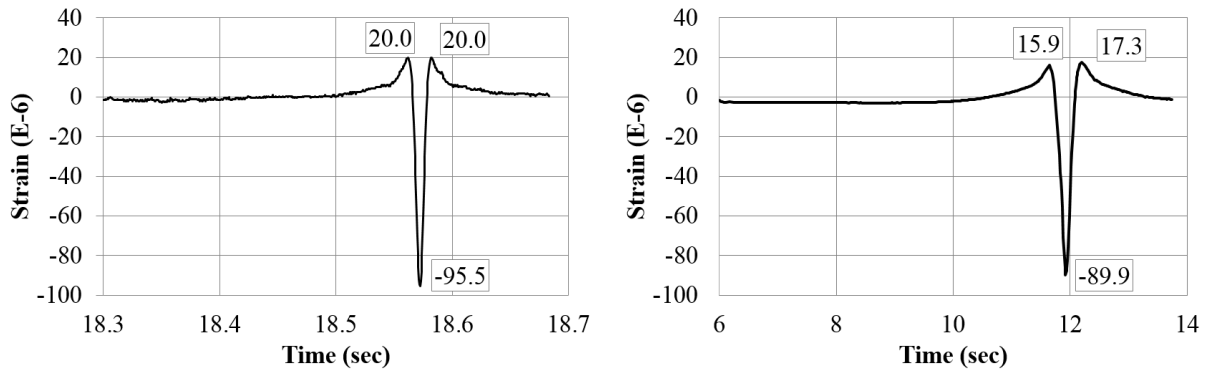
Figure 6.5. Comparison between Test Data (left) and Modeling Data (right) for Longitudinal Strain in Rail Web

6.3.3. *Vertical Strain in the Rail*

The comparison of the vertical strain in the rail is shown in Figure 6.6. The shapes of the two curves exhibited similarities to a high extend. Both the field and the modeling data decreased and reached a maximum compressive strain as the wheel approached, indicating a compressive load in the rail, and started to increase after the passage of the wheel. The FE model gave a maximum compressive strain value of -0.142 millistrain which was 2.16% different from -0.139 millistrain recorded from the field. Therefore, the comparisons between the numerical solutions and the field data demonstrated that the FE model was capable of representing longitudinal behaviors of the railway track structure under a dynamic wheel loading; thus, the validated FE model could be used for further analysis.
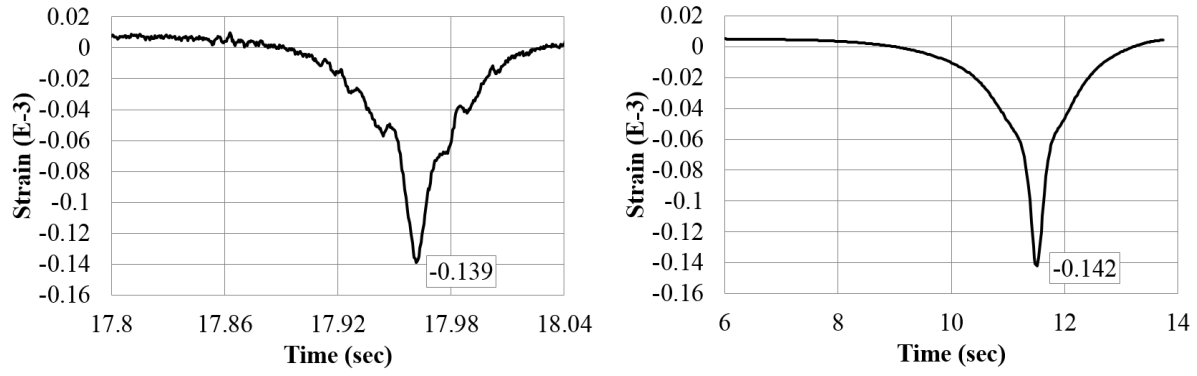
Figure 6.6. Comparison between Field Data (left) and Modeling Data (right) for Vertical Strain

in Rail

CHAPTER 7

PARAMETRIC STUDIES

A series of parametric studies were conducted using each of the validated FE model to investigate the behaviors of track system under impact and longitudinal loads independently.

7.1. *Parametric Study on Impact Load*

For the investigation of track response to impact loads due to wheel flats, two groups of parameters were considered, including the stiffness of rail pad and the speed of train. The stiffness of railpad was related to the vertical modulus and vertical vibration frequency of track system, which potentially affected the response of track to impact loads. In other words, the impact factor, which was the ratio between the maximum impact force and nominal wheel load, could change with the railpad stiffness. The wheel speed, on the other hand, had a direct effect on the rotation-induced impact force as shown in Figure 4.9c, and thus could also affect the behaviors of impact load.

7.1.1. *Railpad Stiffness Results*

According to Harper (1996) and Hepburn (1982), the stiffness of rail pad ranges from 731 kips/inch to 7,320 kips/inch. Three additional cases including 731 kips/inch, 1,924 kips/inch, and 2,747 kips/inch were simulated to compare with the previous case in which a stiffness of 1,370 kips/inch was used as per the manufacturer. The time history of the wheel-rail interaction force corresponding to each case is shown in Figure 7.1.
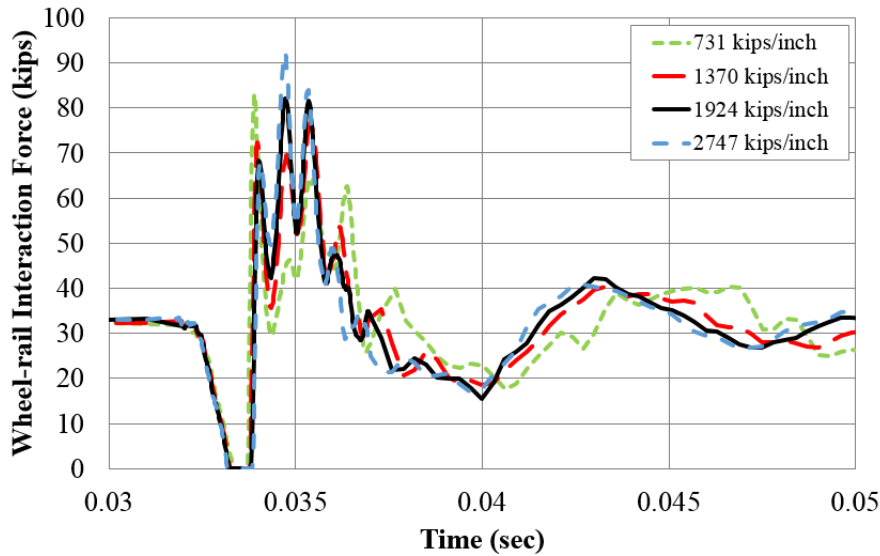
Figure 7.1. Time Histories of Wheel-rail Interaction Force with Rail Pads of Four Different Stiffness

It can be realized that softer rail pads were able to attenuate vibration-induced peak loads yet failed to reduce the direct impact load. Compared to stiff pads, soft pads allowed for larger vertical rail deflection, causing the rail to bend more. As the flat spot passed over the rail, the loss of contact between the rail and wheel gained the rail an upward action (Figure 4.9b). The larger rail deflection allowed by soft rail pads would result in a higher rail unbend acceleration. Therefore, a higher force could be incurred when the wheel and rail collided (Figure 4.9c). In contrast to the increase in the direct impact load, vibration-induced peak loads were reduced as softer rail pads attenuated the vibrational interactions between the rail and concrete crosstie. When the stiffness was increased to 2,747 kips/inch, an exact opposite behavior of impact loads to the case with softer pads was observed. Stiffer rail pads were able to attenuate the direct impact load; however, the vibration-induced peak loads increased significantly.

In order to quantify the effect of rail pad stiffness on the impact factor, that is, the ratio between the maximum impact load and nominal wheel load, their relationship is illustrated in Figure 7.2. Rail pads with a stiffness of 1,370 kips/inch provided best impact attenuation with an impact factor of 2.35. Even though softer pads reduced vibration-induced peak loads, the impact factor was increased to 2.56. Stiffer rail pads further increased the value to 2.53 and 2.84.
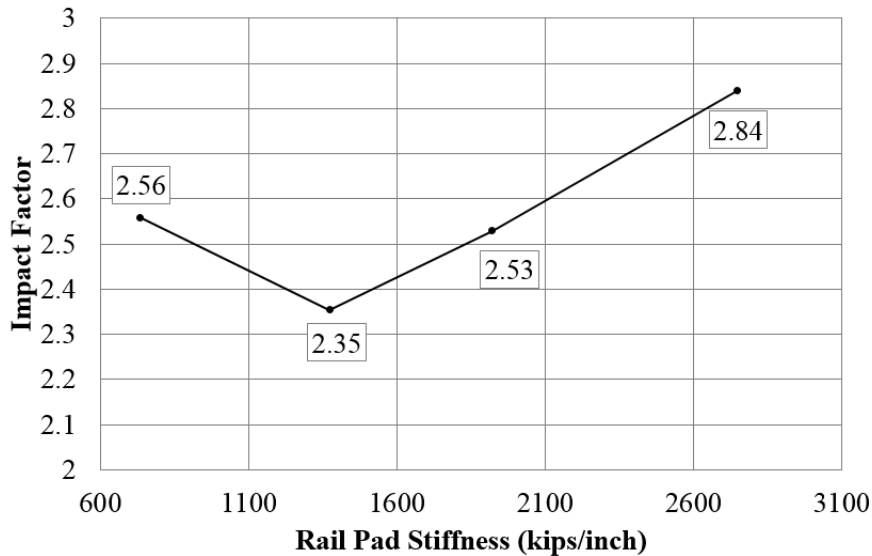
Figure 7.2. Effect of Rail Pad Stiffness on Impact Attenuation

According to Dean et al. (1983) who did a single tie impact test which utilized a drop hammer to produce impact loading, softer pads led to significant reductions in impact factor. Dukkipati and Dong (1999) reached the same conclusion using FE analysis and the stiffness values used in their study were 1,142 kips/inch and 4,854 kips/inch. Their observations agree with the right (ascending) branch of the curve in Figure 7.2. With the results gained from this

study, it was made aware that the selection of rail pad with small stiffness should be made with extra caution.

7.1.2. *Speed Results*

In addition to the rail pad stiffness, the speed of a train can also have an effect on impact factor. To compare with the previous case in which the wheel had a speed of 45 mph, three higher speeds of 90 mph, 120 mph, and 225 mph were simulated. As presented in Figure 7.3, impact factor kept increasing with increasing train speed. As illustrated in Figure 4.9c, the wheel-rail impact was essentially the collision between the edge of wheel flat and rail. In other words, the impact force was resulted from both rotation-induced force and rail unbend force. A higher train speed directly increased the force induced by wheel rotation, and thus, led to higher impact load at the time of wheel-rail impact.
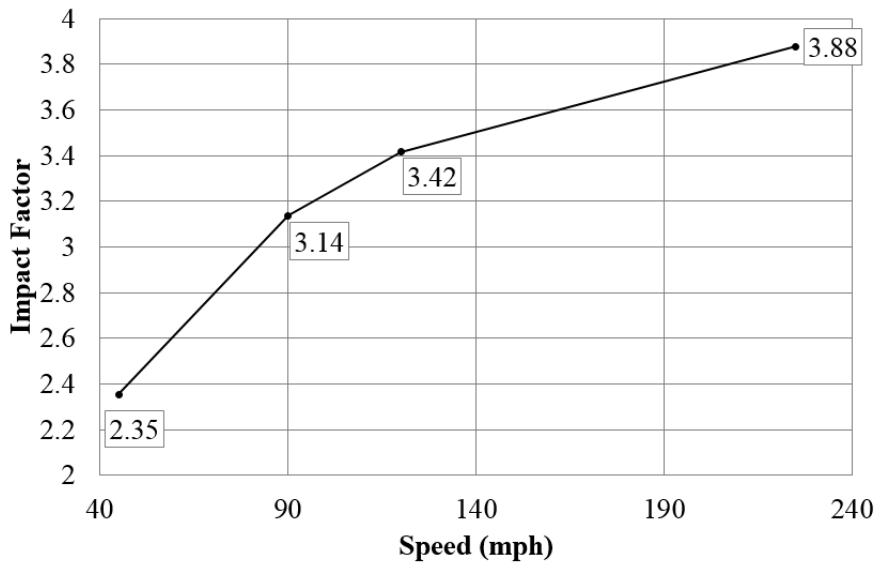
Figure 7.3. Effect of Speed on Impact Factor

In addition, vibration-induced impact loads diminished at high train speeds. Figure 7.4 presented the time history of wheel-rail interaction force when the speed of train was 120 mph. The profile of vibration-induced impact load was not as conspicuous as at a lower speed (Figure 7.1). Its magnitude was only 54 kips and was 29% lower than when the speed was 45 mph. The loss of wheel-rail contact prior to impact was much shorter at high speeds, which averted most of the unbend action of the rail (Figure 4.9). Consequently, the vibration of the track was alleviated, hence fiddling loads from track vibration.
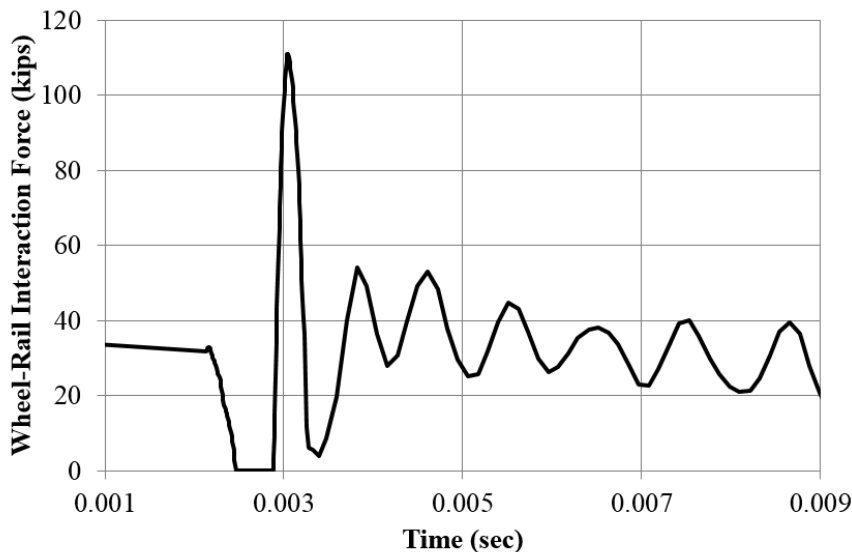
Figure 7.4. Time History of Wheel-rail Interaction Force at 120 mph Train Speed

7.2. *Parametric Study on Longitudinal Load*

Four groups of parameters were investigated for their effects on the distribution of longitudinal loads at the rail and railpad interface. The parameters included the acceleration of wheel, the elastic modulus of clips, the COF between rail and railpad, and the spacing of crossties. A higher acceleration of wheel led to a greater wheel-rail longitudinal force and could affect both the distribution and maximum longitudinal force at the rail-railpad interfaces. The

60

modulus of elasticity of clips determined the clamping force that was produced, and a greater clamping force was likely to increase the longitudinal load capacity of a railseat. Similarly, the COF between the rail and railpad determined the maximum longitudinal force that could be experienced by a railseat. In other words, if the COF increased, the longitudinal load capacity of a railseat increased as well. Different crosstie spacing could change the distribution of vertical wheel load at railseats, which would further affect the distribution of longitudinal forces.

A series of parametric studies were conducted using the validated FE model. The parameters include the acceleration of wheel, elastic modulus of the clips, COF between the rail and railpads, and spacing between crossties. After the model was validated with an acceleration input of 4.81 $inch/sec^2$, 30 $inch/sec^2$ was applied to all cases other than the group of wheel acceleration in the parametric study. The higher acceleration was deemed to represent a more critical case as it could exert greater longitudinal force in the rail.

7.2.1. Wheel Acceleration Results

The acceleration of a train is highly dependent on the power of its locomotives, the total weight of the train, and the maximum adhesion between the locomotive wheels and rail. The acceleration of the train in the field experimentation was 4.81 $inch/sec^2$. In order to investigate the cases where the longitudinal force between the wheel and rail was larger, additional accelerations of 12.5, 20, and 30 $inch/sec^2$ were simulated.
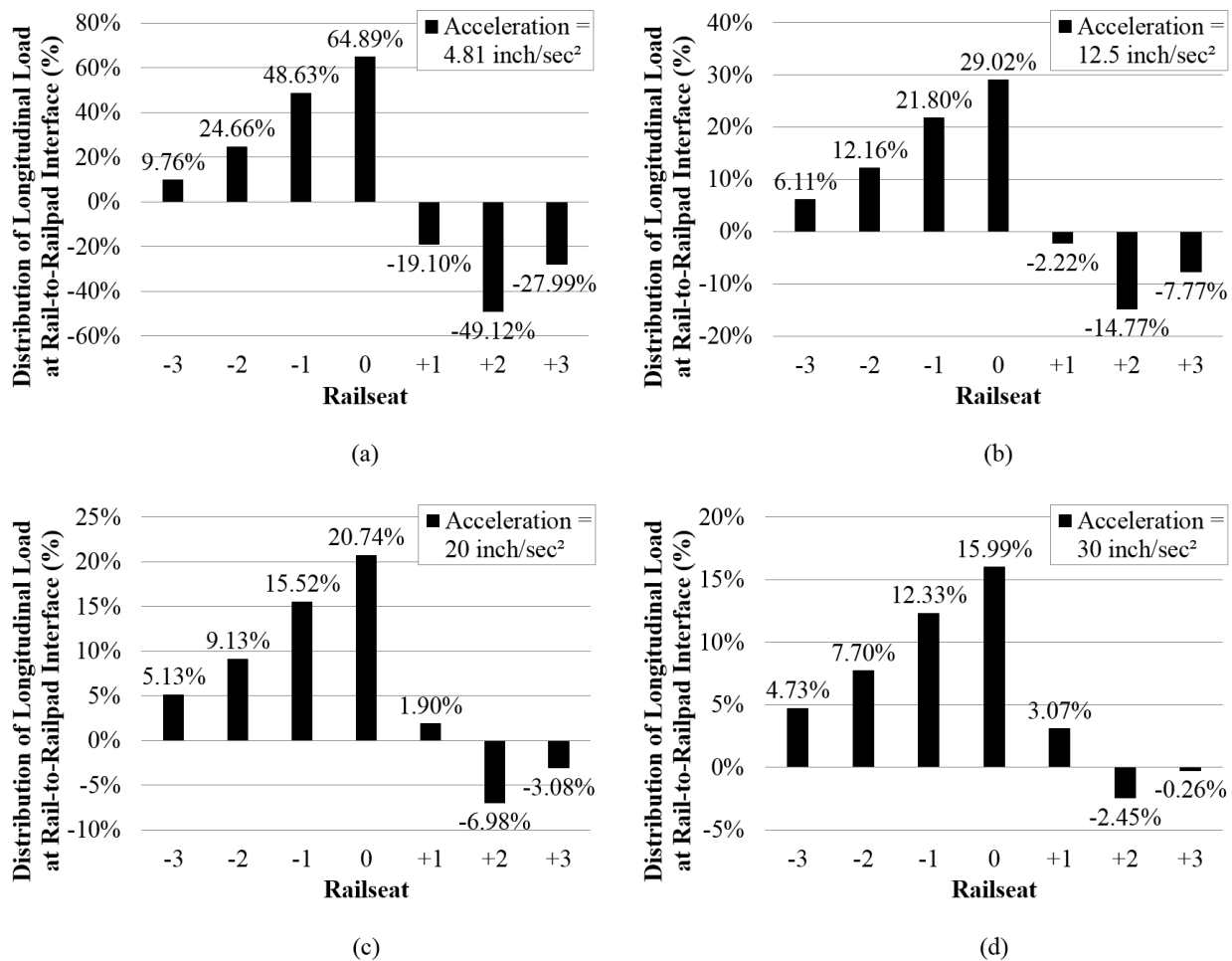
Figure 7.5. Distribution of Longitudinal Load for Rail-to-Railpad Interfaces at the Center Seven Crossties at Wheel Accelerations of (a) 4.81 inch/sec^2, (b) 12.5 inch/sec^2, (c) 20 inch/sec^2, and (d) 30 inch/sec^2

Figure 7.5 compares the percent distributions of longitudinal load between the rail and railpads for the center seven railseats for the four different cases of wheel accelerations. The railseat numbered zero is the 22nd railseat located at the center of the modeled track (Figure 3.3). It could be observed that the longitudinal force was more concentrated to the railseats in the vicinity of the wheel at low acceleration. As wheel acceleration increased, the distribution

62

became less skewed towards the center railseat. Higher accelerations caused the rail to displace more in its longitudinal direction, imparting more longitudinal force to the far railseats.

The values of percent distribution were negative at the railseats where the railpad exerted longitudinal force opposite to the direction the wheel traveled on the rail. This observation can be explained by Figure *6.4*. Before the wheel reached a railseat, the longitudinal displacement of the railpad was positive, hence a positive longitudinal force on the railpad from the rail. Therefore, the longitudinal force exerted on the bottom of the rail by the railpad was negative. As shown in Figure 7.5, the percent distribution of the negative forces decreases with increasing wheel accelerations. The reason was that higher wheel accelerations caused the rail to displace more towards the negative direction, therewith reduced the positive displacement resulted from the effect of vertical bending.
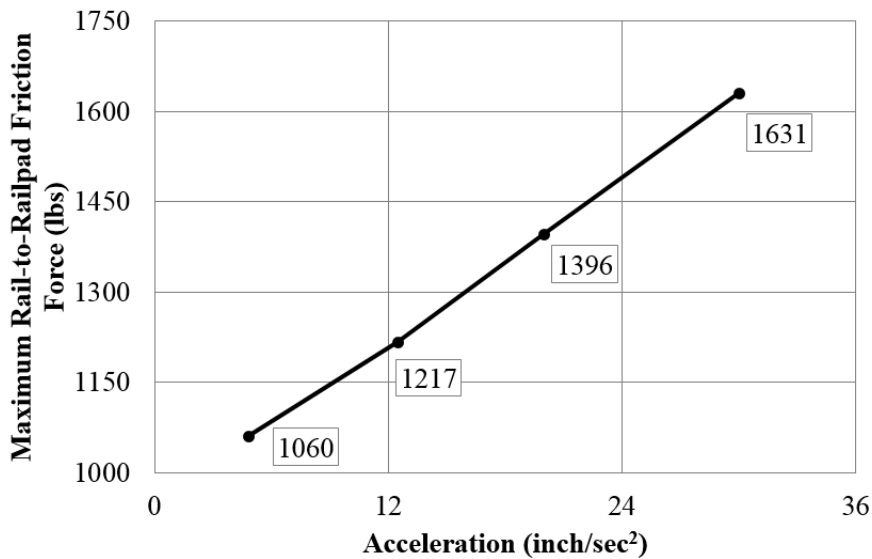
Figure 7.6. Relationship between Acceleration and Maximum Friction Force at Rail-railpad Interface

In addition to the percent distribution of the longitudinal force between the rail and railpad, the relationship between its maximum value and the wheel acceleration was also investigated. As shown in Figure 7.6, the maximum longitudinal force at the rail-to-railpad interface increases linearly with wheel acceleration. However, the percent increase in the maximum longitudinal force was only 54% while the acceleration increased by more than five times. It agreed with Figure 7.5 that the percent distribution decreased at the center railseat even though the force transmitted to it increased; and this behavior could be attributed to the high rigidity of the rail in the longitudinal direction. In other words, the major portion of the longitudinal force produced by the wheel at high accelerations was distributed to the far railseats.

7.2.2. *Elastic Modulus of Clips Results*

The modulus of elasticity of the clips has a direct effect on the clamping force applied on the rail which is related to the capacity of longitudinal restraint a railseat has. Four elastic moduli; 20,000,000, 23,000,000, 26,000,000, and 29,000,000 psi; were simulated in the FE model. Figure 7.7 compares for the percent distributions of longitudinal load between the rail and railpads for the center seven railseats for the four different cases of the elastic moduli of clips. The difference in the distribution of longitudinal forces was not inconspicuous among the four cases. A modulus of elasticity of 26,000,000 psi lead to the highest percent distribution of longitudinal force at the center railseat, but only surpassed the lowest value by a wee difference of 0.34 percent points. Therefore, the elastic modulus of clips had little effect of the distribution of longitudinal forces among railseats.
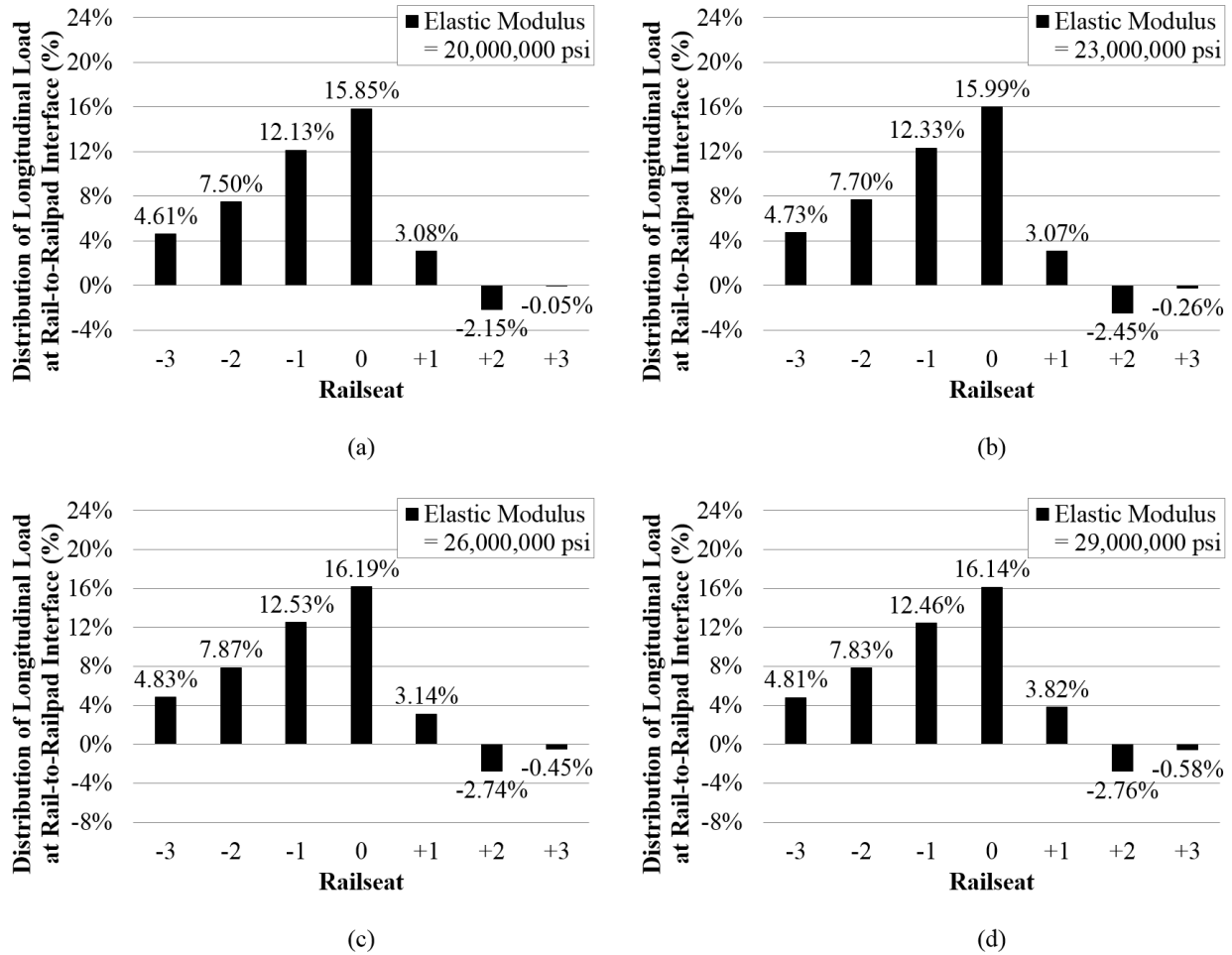
Figure 7.7. Distribution of Longitudinal Load for Rail-to-Railpad Interfaces at the Center Seven Crossties with Clip Elastic Modulus of (a) 20,000,000 psi, (b) 23,000,000 psi, (c) 26,000,000 psi, and (d) 29,000,000 psi

The relationship between the maximum longitudinal force at the rail-railpad interface and modulus of elasticity of clips is illustrated in Figure 7.8. Similar to the observations for the distribution of longitudinal forces, there was almost no changes in the maximum force as the elastic modulus of clips was varied. Additionally, Figure 7.8 suggested that the design of clips could be too conservative as, for this particular train, reducing the elastic modulus from the

design value of 23,000,000 psi to 20,000,000 psi would barely deprive the capacity of longitudinal restraint of fastening system.
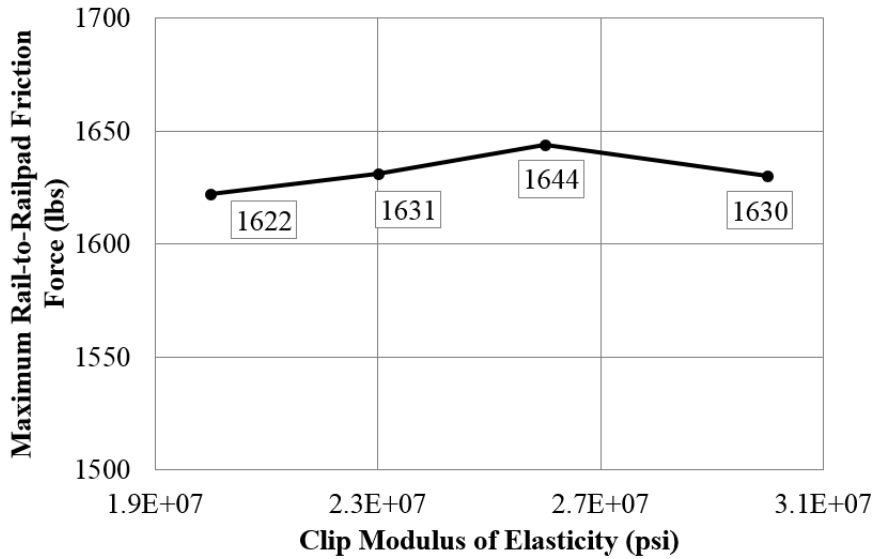
Figure 7.8. Relationship between Clip Elastic Modulus and Maximum Friction Force at Rail-railpad Interface

7.2.3. *Coefficient of Friction between Rail and Railpad Results*

The COF for the contact pair of rail and railpad has a direct effect on the longitudinal restraint a railseat can provide. The COF for the contact between the rail and railpad has a range between 0.12 and 1.5 (Bely et al., 1982; Friedrich, 1986; Yamaguchi, 1990). A total of four COFs; 0.15, 0.30, 0.65, and 1.0 were simulated in the FE model. A COF of 0.15 considered a wet surface condition whereas a COF of 0.30 considered a dry surface condition (Yamaguchi, 1990). The values of 0.65 and 1.0 were included to account for the introduction of various degrees of roughness on the surface of railpads (Bely et al., 1982). As shown in Figure 7.9, the percent distribution of longitudinal force at the center railseat exhibited a considerable increase with COF up to 0.65. No significant change was observed as the COF was raised from 0.65 to

1.0. Therefore, considering the additional efforts required to produce a rougher surface, a COF of

0.65 was deemed most efficient for providing longitudinal restraint for a railseat.
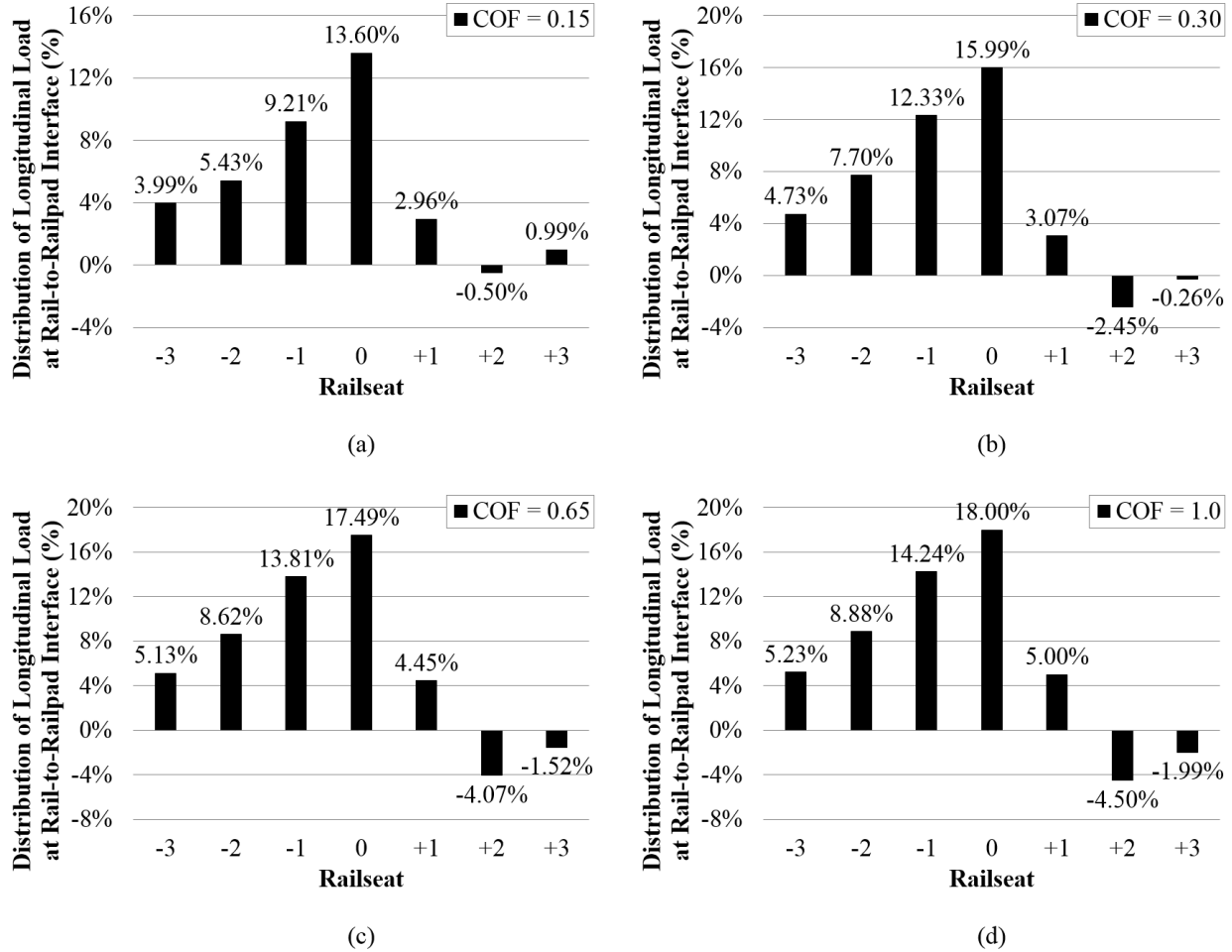
Figure 7.9. Distribution of Longitudinal Load for Rail-to-Railpad Interfaces at the Center Seven Crossties with Rail-to-Railpad COF of (a) 0.15, (b) 0.30, (c) 0.65, and (d) 1.0

The relationship between the maximum longitudinal force at the rail-to-railpad interface and COF between the rail and railpads is presented in Figure 7.10. The maximum force increased with COF; nonetheless, the rate of increase slowed down at high COFs. From a COF of 0.15 to 0.30, the maximum force increased by 20% whereas a mere 3.7% increase in the maximum force

was obtained as the COF increased from 0.65 to 1.0. The observations in Figure 7.10 agreed with those in Figure 7.9 as the gains in the capacity of longitudinal restraint at a railseat was not cost-effective beyond the COF of 0.65.
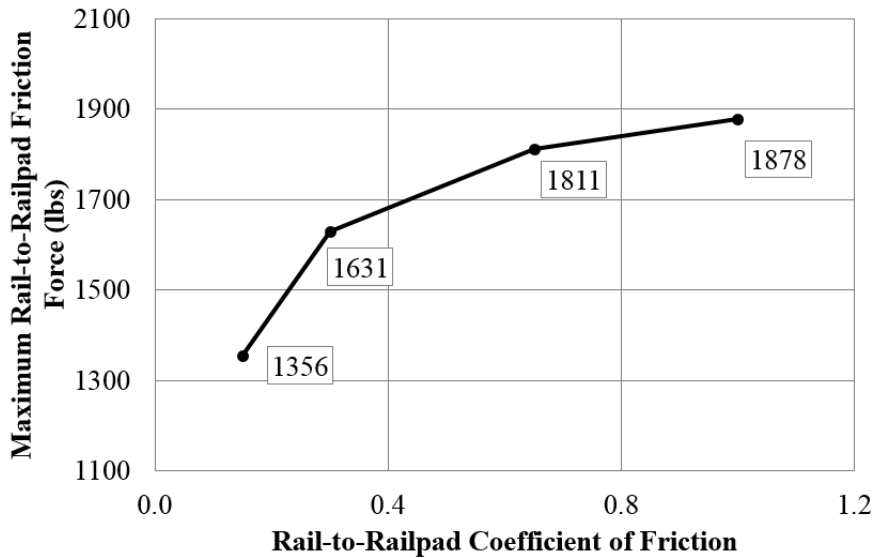
Figure 7.10. Relationship between Rail-to-Railpad COF and Maximum Friction Force at Rail-railpad Interface

7.2.4. Crosstie Spacing Results

For concrete crossties, the center-to-center spacing of crossties in typical practice ranges between 20 inches and 30 inches (AREMA, 2014). The crosstie spacing of the test track in the field experimentation was 24 inches which fell in the middle of the code-specified range. Two additional cases, 20- and 30-inch spacing, were investigated in the FE model to reveal the effects of crosstie spacing on the distribution of longitudinal force.

For crosstie spacing of 20 and 24 inches, the distributions of longitudinal force were similar (Figure 7.11). Small increase was observed at the center railseat while the adjacent railseats underwent small decrease in percent distribution. Nevertheless, a significant increase,

3.86 percent points, only took place at the center railseat as the spacing increased from 24 to 30 inches whereas the distributions at other railseats remained almost the same. The sole increase at the center railseat is deemed related to the increase in vertical loads experienced by the railseats in the vicinity of the wheel due to larger crosstie spacing. Therefore, considering the three crosstie spacing simulated in the FE model, the 24-inch spacing ensured the most uniform distribution of longitudinal force without requiring too small of a spacing.
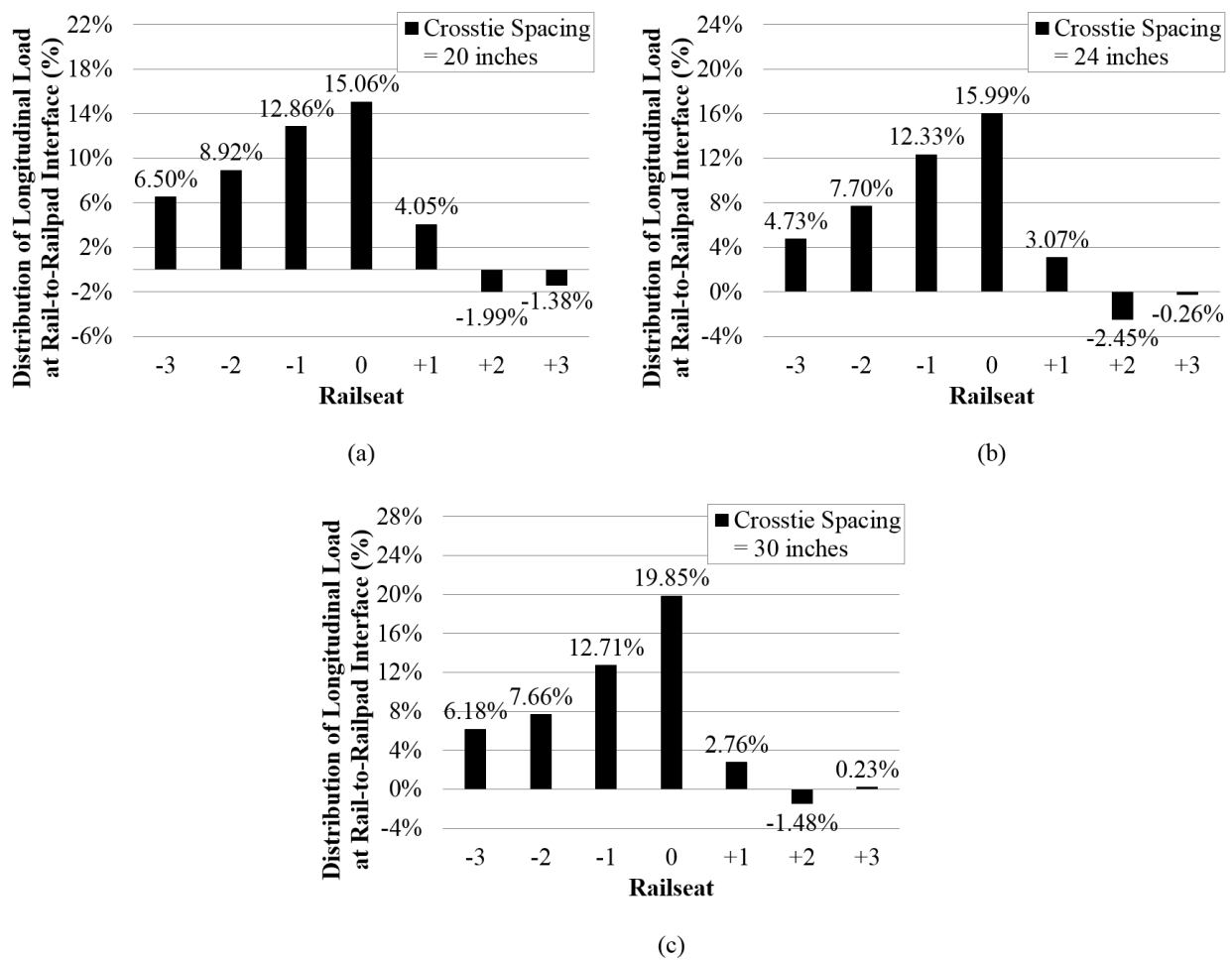
Figure 7.11. Distribution of Longitudinal Load for Rail-to-Railpad Interfaces at the Center Seven Crossties with Crosstie Spacing of (a) 20 inches, (b) 24 inches, and (c) 30 inches

Based on Figure 7.12, the maximum longitudinal force resembled an exponential growth as the crossties were spaced further apart. In other words, increasing the spacing of crossties could potentially impose a severe increase in the demand for longitudinal restraint of fastening system. Therefore, the relationship between the maximum rail-to-railpad longitudinal force and crosstie spacing suggested the significance of imposing an upper limit on the spacing of crossties.
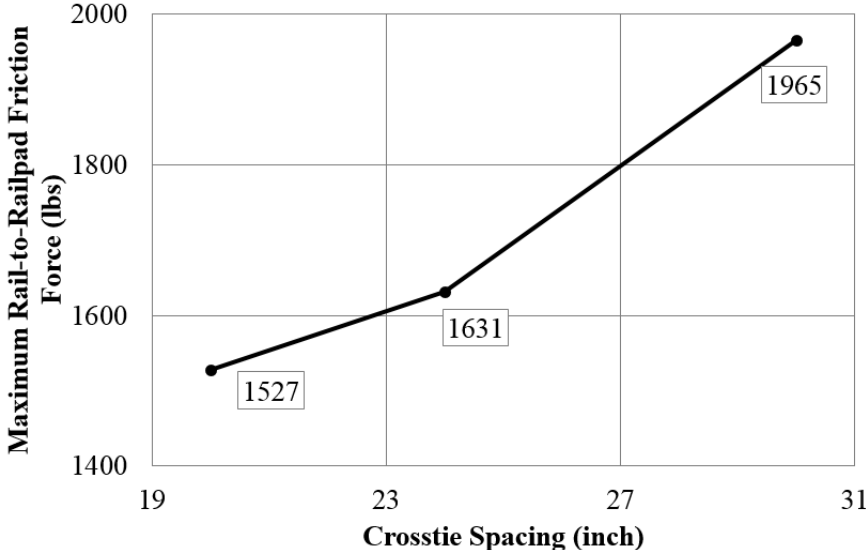
Figure 7.12. Relationship between the Spacing of Crossties and Maximum Friction Force at Rail-railpad Interface

CHAPTER 8

SUMMARY AND CONCLUSIONS

8.1. Summary

FE analysis was employed to investigate the numerical behaviors of railway track system under the influence of rail vehicle dynamic impact load and longitudinal load independently. Two FE models were developed and validated to study each of the two loading scenarios. Parametric studies were conducted using the FE models in an effort to understand the effects of selected system parameters on the behaviors of impact loading and distribution of longitudinal load.

Component-level and single-crosstie calibration were previously performed using experimental and laboratory results by Chen et al. (2014). System-level calibration for each of the two FE models discussed in the pages of the thesis were conducted using experimentation data obtained from field experiments conducted at TTCI in Pueblo, CO. For the FE model on the behavior of impact load due to wheel flat, vertical strain in the rail and internal longitudinal strain in the concrete crosstie obtained from the FE model were compared with the field experimental results with and without the presence of wheel impact independently. Considerable agreements were realized for both the shapes and maximum/minimum values between the numerical and experimental results. For the FE model on the distribution of longitudinal load, comparisons were made for the vertical and longitudinal strains in rail and the longitudinal displacement of railpad between the numerical and experimental results. It was found that the modeling results were able to predict the field behaviors and resemble the experimental results to a high extent. Therefore, both of the FE models were successfully validated and could be used to

71

study the behaviors of track system under the influence of impact load and longitudinal load independently.

Two groups of parameters, including the stiffness of railpad and the speed of wheel, were varied for the numerical analysis on impact load. For the numerical analysis on the distribution of longitudinal load, the acceleration of wheel, the elastic modulus of railpad, the COF between the rail and railpad, and the spacing of crossties were investigated for their relationship with longitudinal loads in the rail fastening system.

8.2. *Conclusions from Impact Load Analysis*

Four different stiffness, between 731 kips/inch and 2,747 kips/inch, were investigated for the effect of rail pad stiffness on impact attenuation. The results indicated rail pad with an intermediate stiffness, 1,370 kips/inch in this case, performed best in attenuating impact load. Rail pad with a lower stiffness, 731 kips/inch, led to an 8.9% increase in the impact factor. An increase of 7.7% in impact factor was also observed for rail pad with a higher stiffness of 1,924 kips/inch. To investigate the relationship between train speed and impact factor, four different speeds, ranging from 45 mph to 225 mph, were simulated in the FE model. It was realized that the increase in impact factor was more significant at lower speeds as opposed to higher speeds. Increasing train speed by twice, from 45 mph to 90 mph, the impact factor was increased by 34%. In comparison, a mere 13% increase was resulted as the train speed was raised by 88%, from 120 mph to 225 mph.

Some additional conclusions can be made based on the results of the FE analysis:

- Impact loading consists of two mechanisms, direct wheel impact and vibration-induced impact;

72

- The location of wheel impact has an effect on the behavior of impact loading, that is, more vibrations are caused in the track system when impact hits the centerline of a crib and thus more severe vibration-induced impact loads, however, this effect is found to be insignificant;

- Direct impact load increases with decreasing rail pad stiffness while vibration-induced impact load increases as rail pad becomes stiffer and an optimized rail pad stiffness exists to reach the highest attenuation of impact loads;

- Impact load increases with increasing train speed.

- Vibration-induced impact load diminishes as train speed increases.

8.3. *Conclusions from Longitudinal Load Analysis*

Based on the results of parametric study from the model of the distribution of longitudinal load, it can be concluded that:

- As the acceleration of wheel increases, the distribution of longitudinal force becomes less skewed as the maximum percent distribution decreases and a larger portion of the longitudinal force is distributed to the far railseats beyond the center seven.

- The maximum longitudinal force between the rail and railpad increases linearly with wheel acceleration.

- The modulus of elasticity of clips has little effect on the distribution of longitudinal force, suggesting the potential surplus in the elastic modulus of clips regarding the demand for longitudinal restraint.

- The increase in COF between the rail and railpad causes a larger portion of the longitudinal force to converge to the center railseat, essentially increasing the capacity of

longitudinal restraint of fastening system. Additionally, a COF of 0.65 is deemed most

efficient in maximizing the longitudinal restraint provided at a railseat.

- Significant increase in the distribution of longitudinal force at the center railseat takes

  place as the spacing of crossties increases beyond 24 inches, suggesting that 24-inch

  spacing for crossties allows for most uniform distribution of longitudinal force without

  requiring too small of a spacing.

- The maximum longitudinal force between the rail and railpad increases exponentially

  with the spacing of crossties.

8.4. *Recommendations*

8.4.1. *Improved Component Design for Optimal Impact Attenuation*

Based on the FE analysis for the relationship between impact load due to wheel flat and

stiffness of railpad, it was realized that an intermediate stiffness, 1370 kips/inch, led to the most

desired impact attenuation result at a speed of 45 mph. For the modeled railpad, the stiffness

corresponded to an elastic modulus of 7,500 psi which happened to be the design value of the

railpad. The attenuation of impact was achieved by attenuating both direct and vibration-induced

impact loads. It was also observed that with increasing stiffness of railpads, vibration-induced

impact load increased whereas direct impact load decreased. As vibration-induced impact load

diminished at higher speeds, the attenuation of impact load would become the sole effort to

reduce direct impact load. It was thus likely that increasing the modulus of elasticity of the

railpad to be greater than 7,500 psi would reduce the resulting impact load. However, stiff

railpads would result in high vertical track stiffness, leading to increased needs on track

maintenance due to wear and fatigue of the track components caused by the augmented dynamic

forces on the rail (Real et al., 2012). Real et al. (2012) also pointed out that excessive vertical

74

track stiffness would induce higher accelerations of the train, reducing the passenger comfort. Therefore, in the design process, considerations are needed to balance between increasing the stiffness of railpad and limiting vertical accelerations of train in order to minimize the cost of maintenance.

8.4.2. *Improved Capacity of Longitudinal Restraint of Rail Fasteners*

As previously discussed, the distribution of longitudinal load at the locations of railseat exhibited insignificant changes regardless of the modulus of elasticity of clips. Additionally, the maximum rail-to-railpad friction force throughout the passage of the wheel exhibited little change with the elastic modulus of clips. The observations suggested that the design clamping force was more than sufficient regarding the longitudinal restraint it provided at a railseat. In the modeled track, the design modulus of elasticity of clips was 23,000,000 psi. Based on the modeling results, reducing the modulus of elasticity by 13%, from the design value to 20,000,000 psi, led to almost no reduction in the capacity of longitudinal restraint of the railseat. Therefore, from the mere perspective of longitudinal restraint, rail clips is allowed to be manufactured using less stiff material, which can lead to lower manufacturing costs and less effort for field installation.

In addition to the modulus of elasticity of clips, the COF between the rail and railpad was another parameter that, upon modifications, could increase the capacity of longitudinal restraint of the railseat. Previous abrasion tests by Kernes et al. (2012) suggested a COF of 0.3 between the rail and railpad under dry field conditions. However, the COF could decrease to as low as 0.15 if moist entered the contact interface (Yamaguchi, 1990; Stachowiak & Batchelor, 2005). And according to the modeling results, significant loss in the capacity of longitudinal restraint was resulted as the COF decreased from 0.3 to 0.15. The maximum friction force experienced at

a railseat underwent a 17% reduction. Furthermore, a COF of 0.65 improved the capacity by 11% compared to the case in which a COF of 0.3 was used. However, no significant further improvement was exhibited as the COF increased from 0.65 to 1.0. The observations thus indicated a considerable enhancement to the capacity of longitudinal restraint of the railseat by increasing the design COF between the rail and railpad from 0.3 to 0.65; and it could be achieved by roughening the surface of railpad (Bely et al., 1982).

8.5.   *Future Work*

The parameters considered in this study for investigating the behavior of impact load due to wheel flat included only the speed of train and the stiffness of railpad. In order to provide a more comprehensive understanding about impact loads, other parameters such as the wheel load applied and thickness of railpad can be included. Additionally, as concrete crossties are more prone to excitation with the presence of gap between the ballast and crosstie, assessing the effect of gaps can be a significantly complementary the study.

In this study, longitudinal load was considered solely with the absence of other longitudinal stress. As aforementioned, buckling due to longitudinal stress can be a combined effect of thermal stress, vehicle loads, and reduced track lateral resistance. Therefore, in addition to vehicle-induced longitudinal force, applying thermal load as well as an initial lateral misalignment in the modeled track allows for the assessment of the relationship between track parameters and track buckling stress and temperature.

REFERENCES

American Railway Engineering and Maintenance-of-Way Association (AREMA). (2014). *AREMA Manual for Railway Engineering.* Lanham, MD 29706: American Railway Engineering and Maintenance-of-Way Association.

Anderson, E., Berg, M., & Stichel, S. (2004). *Rail Vehicle Dynamics.* KTH Railway Technology.

Bely, V. A., Sviridenok, A. I., & Petrokovets, M. I. (1982). *Friction and Wear in Polymer-Based Materials.* Elsevier.

Bian, J., Gu, Y., & Murray, M. (2013). Numerical Study of Impact Forces on Railway Sleepers under Wheel Flat. *Advances in Structural Engineering*, 127-134.

Carvalho, J., Delgado, J., Calcada, R., & Delgado, R. (2013). A New Methodology for Evaluating the Safe Temperature in Continuously Welded Rail Tracks. *International Journal of Structural Stability and Dynamics*.

Chen, Z., Shin, M., Andrawes, B., & Edwards, J. (2014). Parametric study on damage and load demand of prestressed concrete crosstie and fastening systems. *Engineering Failure Analysis*, 49-61.

Dassault Systemes Simulia Corp. (2013). *ABAQUS Analysis User's Manual, Version 6.13.*

Dean, F., Harrison, H., Prause, R. H., & Tuten, J. M. (1983). *Investigation of the Effects of Tie Pad Stiffness on the Impact Loading of Concrete Ties in the Northeast Corridor.* Washington, D.C.: Federal Railroad Administration, Office of Research and Development.

do Carmo, T. B. (2014). *Multifaceted Approach for the Analysis of Rail Pad Assembly Response (M.S. Thesis).* Urbana, IL 61801: University of Illinois at Urbana-Champaign.

Doyle, N. F. (1980). *Railway Track Design: A Review of Current Practice.* BHP Melbourne Research 301 Laboratories, Bureau of Transport Economics.

Dukkipati, R., & Dong, R. (1999). Impact Loads due to Wheel Flats and Shells. *Vehicle System Dynamics*, 1-22.

Esveld, C. (2001). *Modern Railway Track.* Zaltbommel, the Netherlands: MRT Productions.

Foutch, D. A., Kim, T., Otter, D. E., & Doe, B. E. (2006). Investigation of Longitudinal Forces in a Concrete Railroad Trestle. *Journal of Bridge Engineering, 11*(5), 618-625.

Friedrich, K. (1986). *Friction and wear of polymer composites.* Amsterdam: Elsevier.

Grasse, J. S. (2013). *Field Test Program of the Concrete Crosstie and Fastening System (M.S. Thesis).* Urbana, IL 61801: University of Illinois at Urbana-Champaign.

Gustavson, R. (2002). *Structural behaviour of concrete railway sleepers (PhD Thesis).* Sweden: Department of Structural Engineering, Chalmers University of Technology.

Harper, C. (1996). *Handbook of plastics, elastomers, and composites (3rd ed.).* New York: McGraw-Hill.

Hay, W. W. (1982). *Railroad Engineering (2nd Edition).* New York, New York: John Wiley & Sons, Inc.

Hepburn, C. (1982). *Polyurethane elastomers.* London: Applied Science.

Huang, H., & Tutumluer, E. (2011). Discrete Element Modeling for Fouled Railroad Ballast. *Construction and Building Materials*, 3306-3312.

Kaewunruen. (2007). *Experimental and numerical studies for evaluating dynamic behaviour of prestressed concrete sleepers subject to severe impact loading (PhD Thesis).* Australia: School of Civil, Mining, and Environmental Engineering.

Kaewunruen, S., & Remennikov, A. M. (2007). Investigation of free vibrations of voided concrete sleepers in railway track system. *Proceedings of the Institution of Mechanical Engineers, Part F: Journal of Rail and Rapid Transit*, (pp. 495-507).

Kaewunruen, S., & Remennikov, A. M. (2009). Progressive impact behaviour of prestressed concrete sleepers. *Engineering Structures*, 2460-2473.

Kaewunruen, S., & Remennikov, A. M. (2010). Dynamic Properties of Railway Track and Its Components: Recent Findings and Future Research Direction. *Insight: Non-destructive Testing & Condition Monitoring*, 20-22.

Kernes, R. G., Edwards, J. R., Dersch, M. S., Lange, D. A., & Barkan, C. P. (2012). Investigation of the Dynamic Frictional Properties of a Concrete Crosstie Rail Seat and Pad and Its Effect on Rail Seat Deterioration (RSD). *Proceedings of the Transportation Research Board 91st Annual Meeting.* Washington, D.C.

Kerr, A. (2003). *Fundamentals of railway track engineering.* Omaha, NE: Simmons-Boardman Books.

Kish, A. (2011). On the Fundamentals of Track Lateral Resistance. *Proceedings of the AREMA 2011 Annual Conference.* Minneapolis, MN: AREMA.

Kumar, D. K., & Sambasivarao, K. (2014). Static and Dynamic Analysis of Railway Track. *International Journal of Engineering Research and General Science*, 662-671.

LBFoster. (n.d.). *Fastening Systems*. Retrieved from CXT Concrete Crossties: http://www.cxtconcreteties.com/fastening_systems.asp#mstto=

National Academy of Sciences (U.S.). (1976). *Report of the National Academy of Sciences.* National Research Council.

Nguyen, K., Goicolea, J. M., & Galbadon, F. (2011). Dynamic Analysis of High Speed Railway Track Loads on Ballasted Track. *Proceedings of the Fifth International Symposium on Environmental Vibration.* Chengdu, China.

Nielsen, J. C. (2008). High Frequency Vertical Wheel-rail Contact Forces - Validation of a Prediction Model by Field Testing. *Wear*, 1465-1471.

Railway Applications - Track - Test Methods for Fastening System Part 1: Determination of longitudinal rail restraint. (2002). In *Standard EN1314601:2002.* Brussels: Comitée Européen de Normalistion (CEN).

Real, J. I., Gomez, L., Montalban, L., & Real, T. (2012). Study of the influence of geometrical and mechanical parameters on ballasted railway tracks design. *Journal of Mechanical Science and Technology*, 2837-2844.

Rodes, D., & Coats, B. (2008). Resistance to rail creep – what do rail fastenings really have to do? *Proceedings of the AREMA 2008 Annual Conference.* Salt Lake City, UT.

Romero, M. J., Edwards, J. R., Barkan, C. P., Wilson, B., & Mediavilla, J. (2010). Advancements in Fastening System Design for North America Concrete Crosstie in Heavy-Haul Service. *Proceedings of the AREMA 2010 Annual Conference & Exposition.* Orlando, FL: AREMA.

Ruge, P., & Birk, C. (2007). Longitudinal forces in continuously welded rail on bridgedecks due to nonlinear track-bridge interaction. *Computers and Structures*, 458-475.

Selig, E., & Waters, J. (1994). *Track geotechnology and substructure management.* London: T. Telford.

Stachowiak, G., & Batchelor, A. (2005). *Engineering tribology (3rd ed.).* Amsterdam: Elsevier Butterworth-Heinemann.

Stevens, N. J., & Dux, P. F. (2004). *World Intellectual Property Organisation, International Bureau Patent No. WO2004018772 A1.*

UMKC School of Law. (1945). *SOUTHERN PAC. CO. v. STATE OF ARIZ. EX REL. SULLIVAN.* Retrieved from umkc.edu: http://law2.umkc.edu/faculty/projects/ftrials/conlaw/sopacific.html

Van Dyk, B. J., Dersch, M. S., Edwards, J. R., Ruppert, C. J., & Barkan, C. P. (2014). Evaluation of Dynamic and Impact Wheel Load Factors and Their Application for Design. *Transportation Research Board 93rd Annual Meeting.* Washington D.C.

Van Dyk, B. J., Rapp, C. T., Dersch, M. S., Edwards, J. R., Ruppert, C. J., & Barkan, C. P. (2013). Evaluation of Existing Loading Environment in North America for Improved Concrete Sleepers and Fastening Systems. *Proceedings of the 2013 World Congress of Railway Research.* Sydney, Australia.

Volpe, the National Transportation System Center. (2014). *Track Buckling Research.* Volpe, the National Transportation System Center.

Wakui, H., & Okuda, H. (1999). A study on limit-state design for prestressed concrete sleepers. *Proceedings of JSCE* (pp. 1-25). JSCE.

Wang, N. (1996). *Resistance of concrete railroad ties to impact loading (PhD Thesis).* Canada: University of British Columbia.

Wang, W. J., Shen, P., Song, J. H., Liu, Q. Y., & Jin, X. S. (2011). Experimental Study on Adhesion Behavior of Wheel/Rail under Dry and Water Conditions. *Wear*, 2699-2705.

Williams, B. A., Edwards, J. R., Kernes, R. G., & Barkan, C. P. (2014). Analysis of the Lateral Load Path in Concrete Crosstie Fastening Systems. *Proceedings of the 2014 Joint Rail Conference.* Colorado Springs, CO: JRC2014.

Yamaguchi, Y. (1990). *Tribology of plastic materials: Their characteristics and applications to sliding components.* Amsterdam: Elsevier.

Ye, X., Wang, N., & Mindess, S. (1994). Effect of loading rate and support conditions on the mode of failure of prestressed concrete railroad ties subjected to impact loading. *Cement and Conrete Research*, 1286-1298.

Zarembski, A., & Bell, J. G. (2002, October). Limiting the Effects of High-speed Dynamic Forces on Track Structure. *TR News*, 25-26.